Prerequisites for Application of Finite Element Method to Solution Cavities and Conventional Mines

Shosei Serata
Serata Geomechanics
Berkeley, California

ABSTRACT

There are three basic prerequisites for a successful application of the finite element method to problems of solution cavities and conventional salt mines. The first requirement is to establish the constitutive equations of rock salt and adjacent rock media based on laboratory tensor analysis. The second requirement is a laboratory model technique for analyzing the interaction between the tensor properties of the materials and a given three-dimensional geometry of the underground. By using the laboratory model, the finite element program can be calibrated in regard to the interaction. The third requirement is the field technique of stress-strain distribution analysis of boreholes and mine structures which enables the field evaluation of the finite element program to true underground conditions. Different techniques are developed for the solution cavity and conventional salt mine studies because of the basic difference in the rock mechanics conditions between the two.

INTRODUCTION

The use of the finite element method has become popular in rock mechanics studies during the last five years. Although its application to elastic and some idealized media has proven to be quite effective, its application to viscoelastic and viscoplastic media requires a basic investigation of material properties and geometry effects. The application of the finite element method for solving problems of solution cavities and conventional salt mines in particular requires first, the critical evaluation of the tensor properties of halite, sylvite and adjacent rock media prior to formulating the finite element program. Secondly, laboratory and field calibration of the program is essential before its application to actual underground conditions which are illustrated in Figures 1a and 1b. Without

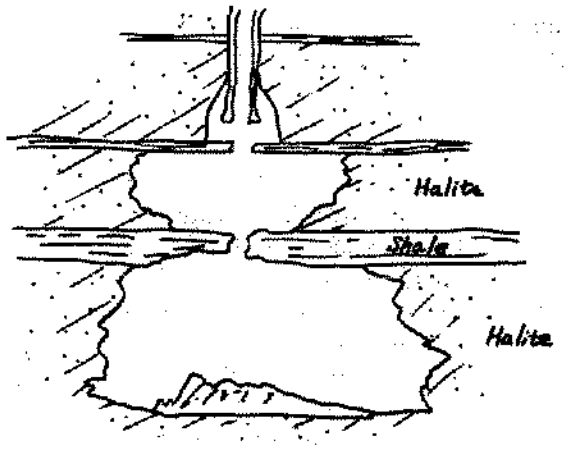

Figure 1a. Typical problems of solution cavities studied by finite element method.

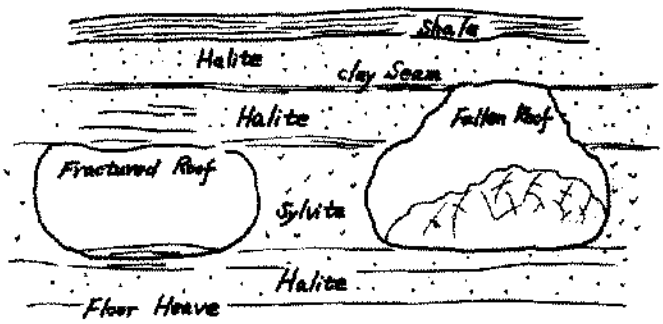

Figure 1b. Typical problems of conventional salt mines studied by finite element method.

this calibration, solutions of the finite element analyses would become numerical games. As a matter of fact, they are often erroneous and misleading.

The objective of this paper is to describe the three basic prerequisites for developing useful finite element programs for solving problems of solution cavities and conventional salt mines. The first prerequisite is to establish the constitutive equations of the materials based on laboratory tensor testing of sample specimens. At least ten fundamental tensor coefficients are needed for establishing the constitutive equations in order to describe the time-dependent behaviors of rock salt under the various stress-strain states; elastic, viscoelastic, viscoplastic and brittle.

Unfortunately, the values of the tensor coefficients have not been accurately determined by those who have attempted to apply the finite element method for solving these problems. For example, the octahedral shearing strength, K_o, of halite is determined to be relatively constant at 650 ± 50 psi under room temperature regardless of the source of the specimen and method of testing. This value was determined by using three radically different tensor testing techniques which were all pioneered in my laboratory. The techniques are the modified transition method, ATT creep method and cylindrical cavity method. The K_o values reported by other investigators vary widely ranging from 80 to 2,500 psi. This wide range reflects the effects of the individual testing methods rather than the material property itself. This may be regarded as an indication of the complexity involved in the determination of the tensor properties of rock salt. The values of the other tensor coefficients are even more uncertain than the K_o value.

The second prerequisite is to have an adequate model testing technique for calibration of the finite element program which is based on the constitutive equations of the materials. The model testing is required for evaluating the coupled effects among the elastic, viscoelastic, viscoplastic and brittle behaviors of rock salt which prevail around the structural boundaries in both solution cavities and conventional mine openings. A model made of a thickwalled cylinder is most useful for this purpose because of its simplicity in mathematical treatment. It is the accuracy of the laboratory model testing that determines the accuracy of the program.

The third prerequisite is a determination of the underground stress field to which the finite element program should be adopted. In solution cavity analysis, deep test wells may be used for the field determination of the stress field. In conventional mine openings, distributions of stress and strain around certain mine structures are measured for the field evaluation.

The basic concept and techniques needed for fulfilling the three prerequisites are described for analyses of both solution cavities and conventional mines. The differences in studying solution cavities and the conventional mines are discussed. Experimental results given here were mostly obtained by using the standard halite from a Texas salt mine.

SALT PROPERTIES AROUND SOLUTION CAVITIES

The structural behaviors of rock salt around solution cavities are uniquely different from those observed in conventional salt mines. The rock salt deforms plastically without brittle fracture even if the cavities are dry and exposed to the atmosphere. This plastic nature of the cavity boundary is due to the three-dimensional geometry of the cavities, as illustrated in Figure 1c.

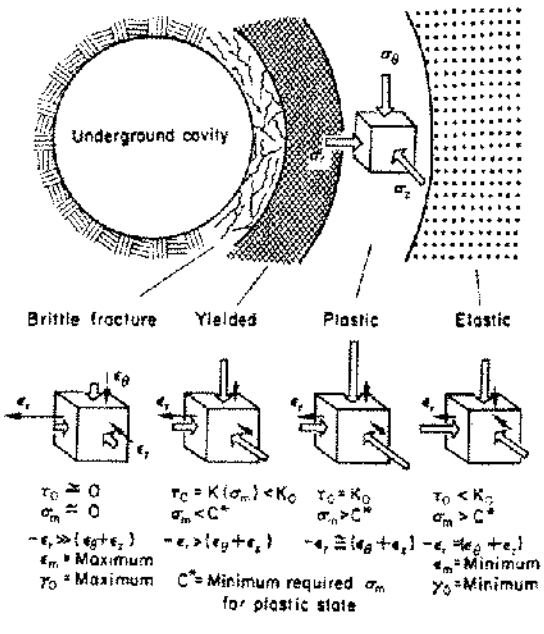

Figure 1c. Various stress-strain states around salt cavity.

Four different stress-strain states develop around an underground cavity regardless of its shape, whether a regular or irregular form. The brittle

fracture zone shown in the figure does not exist if the geometry is an ideal cylinder or sphere. The zone of the brittle fracture may develop only if the shape of the cavity deviates from these ideal forms. Nevertheless, the extent of the brittle fracture zone is limited regardless of the shape of the cavity. This is due to the natural restriction of the lateral earth pressure in relation to the overburden pressure.

The plastic behavior of the cavities is explained by the tensor properties of rock salt which are presented in the $\tau_o - \sigma_m$ diagram of Figure 1d. The

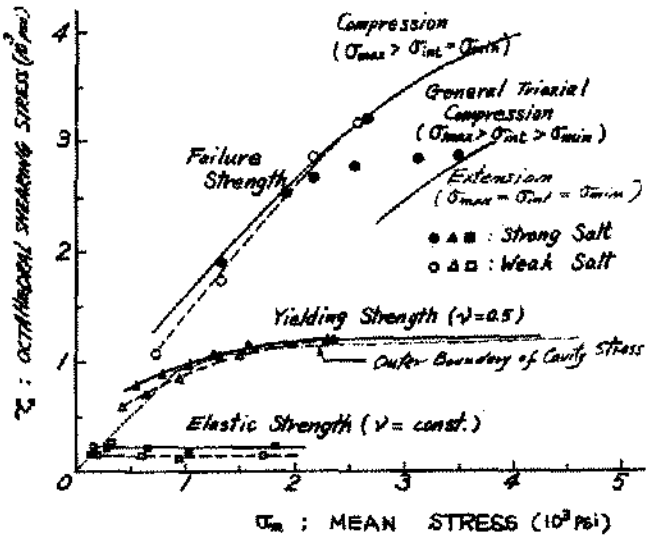

Figure 1d. Potential surfaces of halite determined by tensor testing illustrating stress restriction around salt cavity.

tensor notations are summarized in Figure 2. The three types of curves in the figure describe the failure, yielding and elastic strengths of rock salt in a three-dimensional stress field. The geometry of an underground cavity imposes upon itself the stress restriction which is indicated by the chain line in the diagram. It shows that the stress condition around the cavity transfers from the elastic to plastic states rather suddenly without experiencing the brittle fracture. This transition phenomenon was shown to actually exist under the tensor testing condition of the material, which is illustrated in Figure 3.

The results of the tensor testing of rock salt were then used to formulate the constitutive equations of rock salt in the following numerical forms.

$$\frac{d\epsilon_{ij}}{dt} = \frac{1}{2G_1}\frac{dS_{ij}}{dt} + \frac{S_{ij}}{2\eta_2} - \frac{G_2}{2\eta_2^2} e^{-G_2 t/\eta_2} \int e^{G_2 t/\eta_2} S_{ij}\, dt$$

$$+ \frac{\delta_{ij}}{9K}\frac{d\sigma_{kk}}{dt} + \frac{\sigma_{kk}}{3\eta_2^*}\delta_{ij} - \frac{G_2^*\delta_{ij}}{3\eta_2^{*2}} e^{-G_2^* t/\eta_2^*} \int e^{G_2^* t/\eta_2^*} \sigma_{kk}\, dt$$

The total deformation for any given time, t, becomes:

$$\epsilon_{ij} = \frac{S_{ij}}{2G_1} + \frac{1}{2\eta_2} e^{-G_2 t/\eta_2} \int e^{G_2 t/\eta_2} S_{ij}\, dt$$

$$+ \frac{\sigma_{kk}}{9K}\delta_{ij} + \frac{\delta_{ij}}{3\eta_2^*} e^{-G_2^* t/\eta_2^*} \int e^{G_2^* t/\eta_2^*} \sigma_{kk}\, dt.$$

The deformation rate of the media under the plastic state similarly may be expressed as:

$$\frac{d\epsilon_{ij}^p}{dt} = \frac{1}{2G_1}\frac{dS_{ij}}{dt} + \frac{\delta_{ij}}{9K}\frac{d\sigma_{kk}}{dt} + \frac{1}{2}\left\{\frac{1}{\eta_3}\left(1 - \frac{K_0}{\tau_0}\right) + \frac{1}{\eta_3}\right\} S_{ij}$$

$$- \frac{G_2}{2\eta_3^2\tau_0} e^{-G_2 t/\eta_3} \int \tau_0\, e^{G_2 t/\eta_3}\, dt$$

where

ϵ_{ij} = components of strain tensor
S_{ij} = components of deviatoric stress tensor
G_1 = shear modulus
G_2 G_2^* = retarded moduli in viscoelastic state
G_3 = retarded shear modulus in viscoplastic state
η_2, η_2^* = viscosity coefficients in viscoelastic state
η_3, η_4 = viscosity coefficients in viscoplastic state
K = bulk modulus
σ_{kk} = sum of principal stresses
δ_{ij} = Kronecker delta
τ_0 = octahedral shearing stress
K_0 = octahedral shearing strength

The ten tensor coefficients of the material are determined in the laboratory at room temperature in order to use the above constitutive equations. The coefficients are also determined under elevated temperatures in order to apply the constitutive equations to deep solution cavities where temperatures may reach up to 300°F. The elastic coefficients of K and G were found to be unaffected by temperatures up to 300°F, as shown in Figure 4a. The viscoelastic properties of the halite represented by G_2 and η_2 were also found to be independent of the temperature, as shown in Figure 4b. The octahedral shearing strength K_o of the halite is

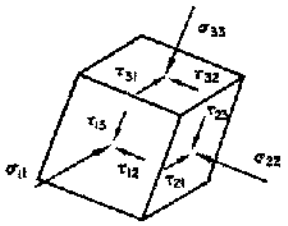

Stress tensors in general orientation

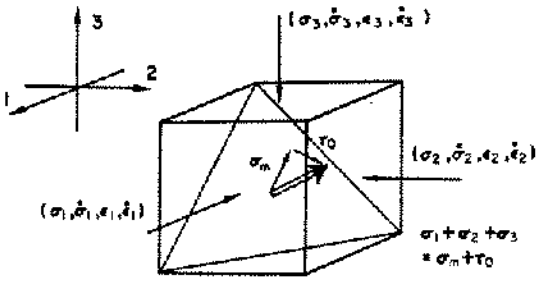

Twelve tensor components in principal orientation

$$S = \begin{bmatrix} \sigma_{11} & \tau_{12} & \tau_{13} \\ \tau_{21} & \sigma_{22} & \tau_{23} \\ \tau_{31} & \tau_{32} & \sigma_{33} \end{bmatrix} = \begin{bmatrix} \sigma_1 & 0 & 0 \\ 0 & \sigma_2 & 0 \\ 0 & 0 & \sigma_3 \end{bmatrix}$$

σ_{ii} = normal stresses
τ_{ij} = shear stresses
σ_i = principal stresses
i, j = notation of repetition.

$$E = \begin{bmatrix} \epsilon_{11} & \frac{1}{2}\gamma_{12} & \frac{1}{2}\gamma_{13} \\ \frac{1}{2}\gamma_{21} & \epsilon_{22} & \frac{1}{2}\gamma_{23} \\ \frac{1}{2}\gamma_{31} & \frac{1}{2}\gamma_{32} & \epsilon_{33} \end{bmatrix} = \begin{bmatrix} \epsilon_1 & 0 & 0 \\ 0 & \epsilon_2 & 0 \\ 0 & 0 & \epsilon_3 \end{bmatrix}$$

ϵ_{ii} = longitudinal strains
γ_{ij} = shear strains
ϵ_i = principal strains.

Stress Rate Tensor

$$\frac{\partial S}{\partial t} = \frac{\partial}{\partial t}\begin{bmatrix} \sigma_{11} & \tau_{12} & \tau_{13} \\ \tau_{21} & \sigma_{22} & \tau_{23} \\ \tau_{31} & \tau_{32} & \sigma_{33} \end{bmatrix} = \frac{\partial}{\partial t}\begin{bmatrix} \sigma_1 & 0 & 0 \\ 0 & \sigma_2 & 0 \\ 0 & 0 & \sigma_3 \end{bmatrix}$$

$$= \begin{bmatrix} \frac{\partial \sigma_1}{\partial t} & 0 & 0 \\ 0 & \frac{\partial \sigma_2}{\partial t} & 0 \\ 0 & 0 & \frac{\partial \sigma_3}{\partial t} \end{bmatrix} = \begin{bmatrix} \dot{\sigma}_1 & 0 & 0 \\ 0 & \dot{\sigma}_2 & 0 \\ 0 & 0 & \dot{\sigma}_3 \end{bmatrix}$$

Strain Rate Tensor

$$\frac{\partial E}{\partial t} = \frac{\partial}{\partial t}\begin{bmatrix} \epsilon_{11} & \frac{1}{2}\gamma_{12} & \frac{1}{2}\gamma_{13} \\ \frac{1}{2}\gamma_{21} & \epsilon_{22} & \frac{1}{2}\gamma_{23} \\ \frac{1}{2}\gamma_{31} & \frac{1}{2}\gamma_{32} & \epsilon_{33} \end{bmatrix} = \frac{\partial}{\partial t}\begin{bmatrix} \epsilon_1 & 0 & 0 \\ 0 & \epsilon_2 & 0 \\ 0 & 0 & \epsilon_3 \end{bmatrix}$$

$$= \begin{bmatrix} \frac{\partial \epsilon_1}{\partial t} & 0 & 0 \\ 0 & \frac{\partial \epsilon_2}{\partial t} & 0 \\ 0 & 0 & \frac{\partial \epsilon_3}{\partial t} \end{bmatrix} = \begin{bmatrix} \dot{\epsilon}_1 & 0 & 0 \\ 0 & \dot{\epsilon}_2 & 0 \\ 0 & 0 & \dot{\epsilon}_3 \end{bmatrix}$$

Octahedral shear stress, τ_0:

$$\tau_0 = \tfrac{1}{3}\sqrt{(\,(\sigma_1 - \sigma_2)^2 + (\sigma_2 - \sigma_3)^2 + (\sigma_3 - \sigma_1)^2\,)}.$$

Octahedral shear strain, γ_0:

$$\gamma_0 = \tfrac{2}{3}\sqrt{(\,(\epsilon_1 - \epsilon_2)^2 + (\epsilon_2 - \epsilon_3)^2 + (\epsilon_3 - \epsilon_1)^2}$$

mean stress: $\sigma_m = \frac{1}{3}(\sigma_1 + \sigma_2 + \sigma_3)$

mean strain: $\epsilon_m = \frac{1}{3}(\epsilon_1 + \epsilon_2 + \epsilon_3)$

Figure 2. Notations of tensor testing of halite.

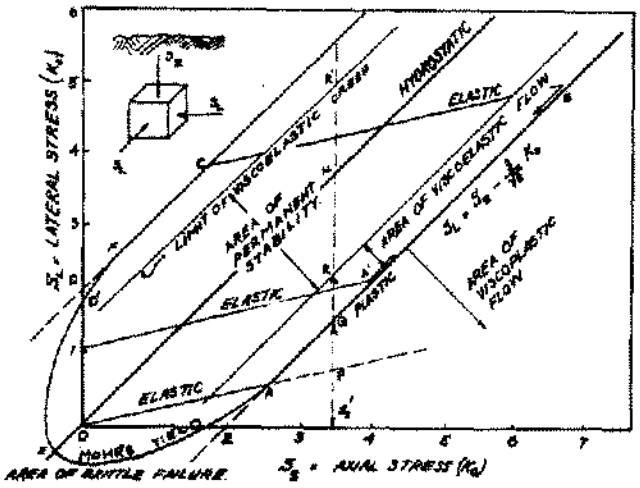

Figure 3a. Theory of transition between elastic and plastic states.

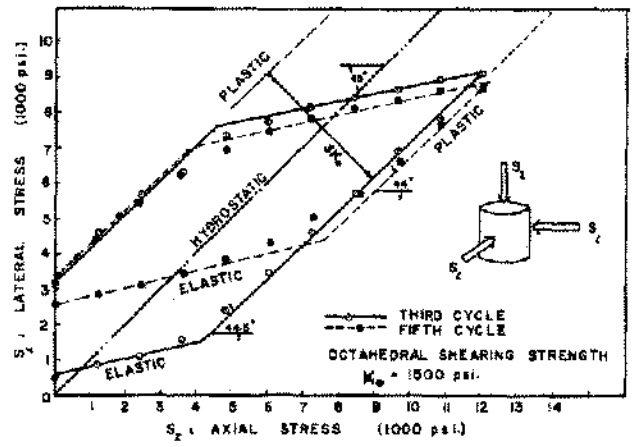

Figure 3b. Experimental proof of transition between elastic and plastic states.

however seriously affected by the temperature, as illustrated in Figure 4c. The most significant effect of temperature was found to be upon the viscoplastic coefficient η_4 of the material, as shown in Figure 4d.

The stress conditions of a cylindrical cavity are determined from the tensor properties of the rock salt. The stress distributions in the yielded, plastic and elastic zones around the cavity are given in the following.

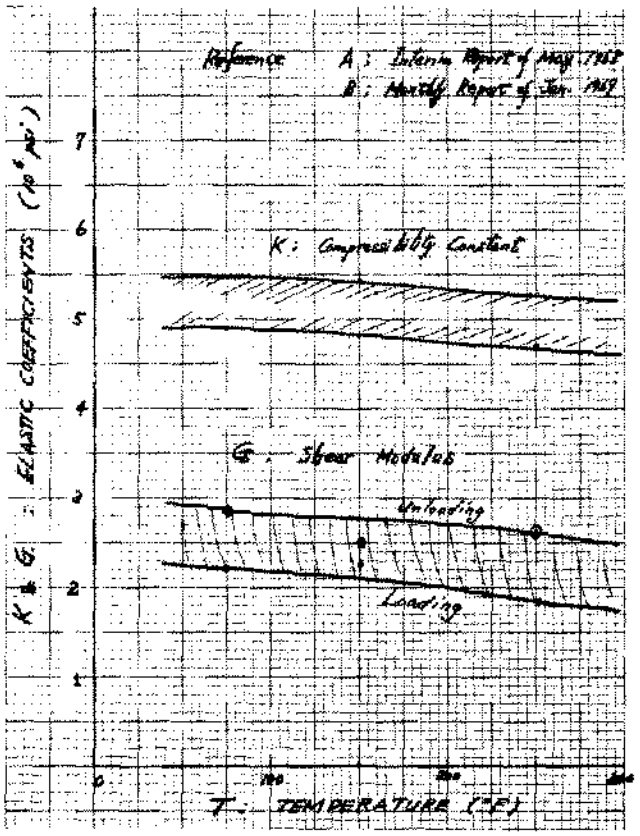

Figure 4a. Effect of temperature on elastic tensor coefficients.

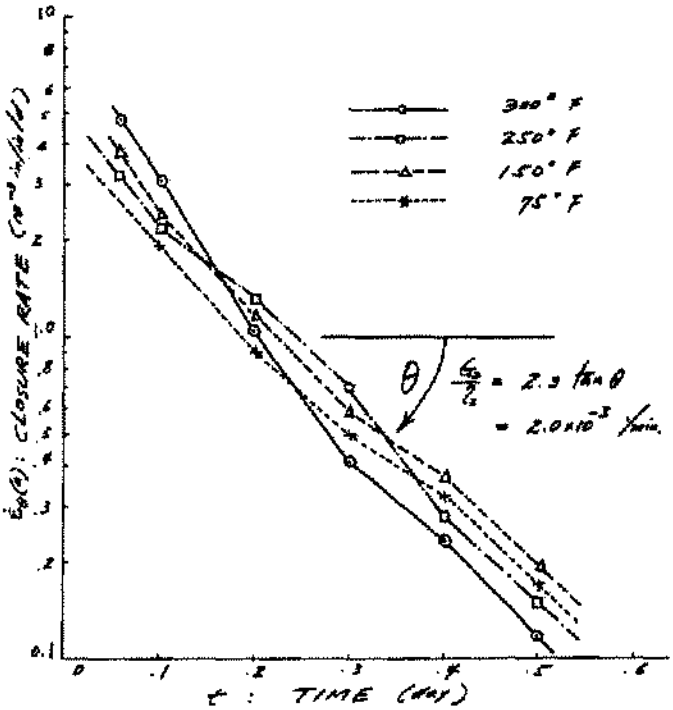

Figure 4b. Effect of temperature on viscoelastic tensor coefficients.

Stress distribution in the yielded zone.

$$\begin{cases} \sigma_r = \dfrac{\beta}{\tan\phi}\left\{\left(\dfrac{r}{a}\right)^n - 1\right\} \\ \sigma_\theta = \dfrac{\beta(1+\tan\phi)}{\tan\phi(1-\tan\phi)}\left\{\left(\dfrac{r}{a}\right)^n - 1\right\} + \dfrac{2\beta}{1-\tan\phi} \\ \sigma_z = \dfrac{\beta}{\tan\phi(1-\tan\phi)}\left\{\left(\dfrac{r}{a}\right)^n - 1\right\} + \dfrac{\beta}{1-\tan\beta} + \sigma_z^{**} \end{cases}$$

Stress distribution in the plastic zone.

$$\begin{cases} \sigma_r = Y^* \ln\left(\dfrac{r}{p}\right) - \dfrac{Y}{2} + \Delta P_L \\ \sigma_\theta = Y^* \ln\left(\dfrac{r}{p}\right) - \dfrac{Y}{2} + \Delta P_L + Y^* \\ \sigma_z = Y^* \ln\left(\dfrac{r}{p}\right) - \dfrac{Y}{2} + \Delta P_L + \dfrac{Y^*}{2} + \sigma_z^{**} \end{cases}$$

Stress distribution in the elastic zone.

$$\begin{cases} \sigma_r = -\dfrac{Y}{2}\left(\dfrac{p}{r}\right)^2 + \Delta P_L \\ \sigma_\theta = \dfrac{Y}{2}\left(\dfrac{p}{r}\right)^2 + \Delta P_L \\ \sigma_z = P_o \end{cases}$$

where

$Y = \sqrt{6K_o^2 - \frac{4}{3}\sigma_z^{*2}}$

σ_r, σ_θ & σ_z = three principal stresses in cylindrical coordinate

$\sigma_z^* = \sigma_z - \dfrac{\sigma_r + \sigma_\theta}{2}$ in the elastic state

p = plastic radius

P_o & P_L = Overburden and lateral earth pressures, respectively.

$Y^* = \sqrt{6K_o^2 - \frac{4}{3}\sigma_z^{**2}}$

$\sigma_z^{**} = \sigma_z - \dfrac{\sigma_r + \sigma_\theta}{2}$ in the plastic state

ϕ = Angle of yield surface to the $\sigma_m = Pi$ line.

β = pure shear strength at internal pressure.

$n = \dfrac{2\tan\phi}{1-\tan\phi}$

$\Delta P_L = P_L - Pi$ = difference between the internal and external pressures.

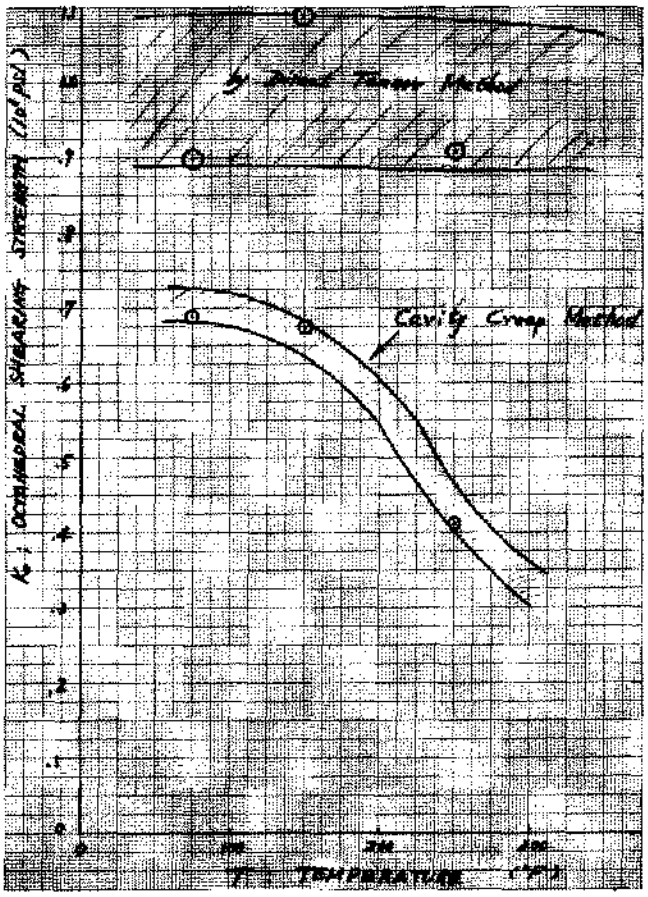

Figure 4c. Effect of temperature on octahedral shearing strength.

The constitutive equations and the tensor coefficients are usually unaffected by prolonged exposure to fluids saturated with the salt. The test specimens which were kept in various liquids for over one month did not show any effect upon the strength of rock salt. The widely reported effect of liquid seems to be erroneous. The liquid exposure of a testing specimen only changes the friction of the loading surface but not the strength of the material. Yet the change in the friction causes a serious reduction in the load-supporting capacity

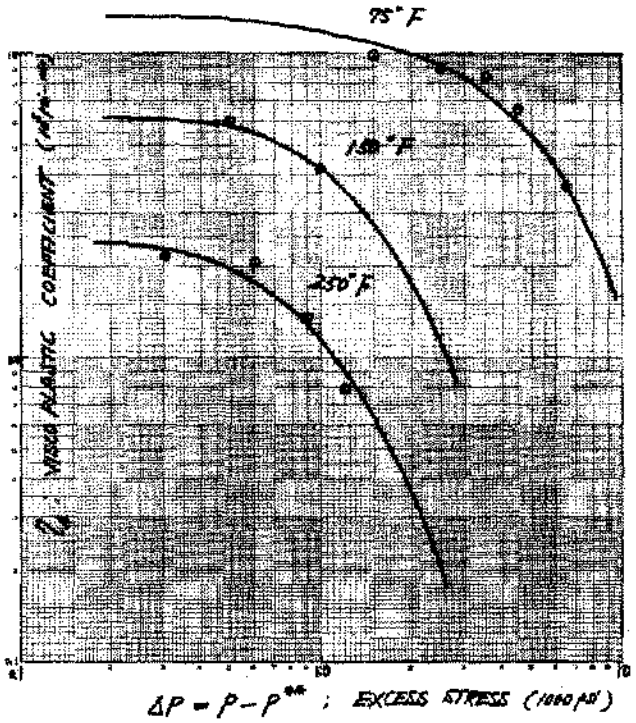

Figure 4d. Effect of temperature on viscoplastic coefficient.

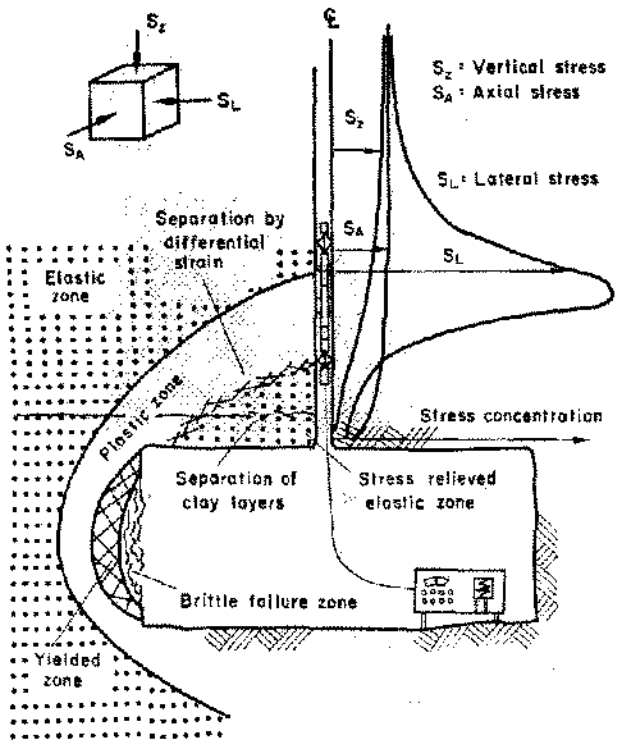

Figure 5a. Development of brittle zones around mine openings.

of the specimen which is independent of the material strength. This laboratory observation has been proven valid in various background solution cavity measurements. The properties of rock salt under the conditions of solution cavities can be determined accurately by using the tensor testing technique.

SALT PROPERTIES IN CONVENTIONAL MINES

The behaviors of rock salt in conventional mine openings are significantly different from those in solution cavities. The difference arises entirely from the geometry difference. Room and pillar structures of mines result in two types of stress states which are not usually found around solution cavities. They are the brittle failure zone and the stress-relieved elastic zone, as illustrated in Figure 5a. Although both zones are formed by different mechanisms, they may cause similar failure hazards to mine safety.

The brittle failure zones which are created on pillar walls are often badly fractured by large unconfined stresses due to the overburden pressure to the pillars. On the other hand, the stress relieved zone is usually not fractured at first. However, it gradually fails by a separation of large roof slabs. This failure is mainly due to the separation between the stress relieved zone and the stress arch. The separation is caused by the sharp differential strain which develops along the lower boundary of the stress arch. Regardless of the difference in the failure process, the brittle grain separation is responsible for both roof and pillar failures which are not usually encountered in solution cavities. The brittle grain separation is shown in the close-up photograph of rock salt under brittle deformation in Figure 5b.

A well-defined boundary between the brittle deformation and viscoplastic yield has been found in both laboratory and underground experiments. The boundary is best described by the yield surface which is in the three principal stress coordinates, as shown in Figure 6a. The shaded cone-shaped surface is the yield surface which forms the critical stress boundary within which no brittle failure is possible. Both brittle and plastic failures take place outside of the yield surface. The plane cross sections of the potential surfaces including the elastic, yielded and failure surfaces show that the brittle failure is seriously affected by the intermediate principal stress, while the viscoplastic flow is not

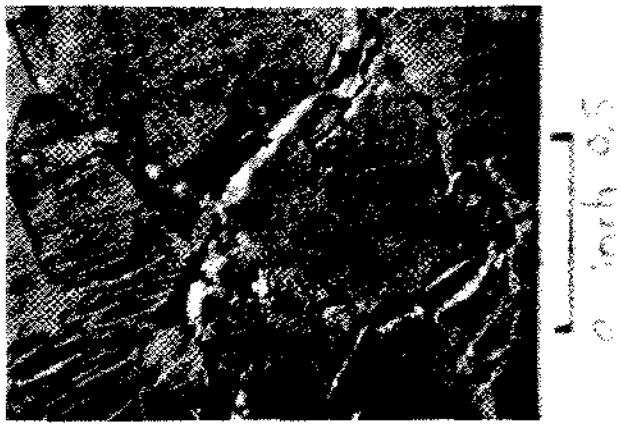

Figure 5b. Grain separation and crystal fracture in brittle deformation.

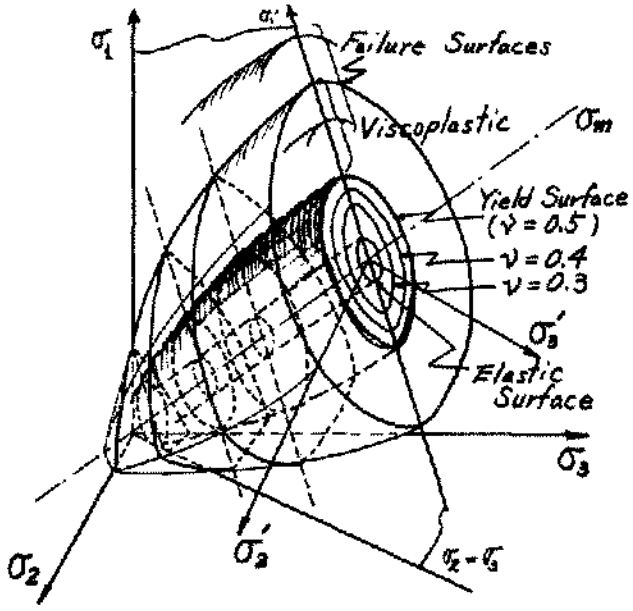

Figure 6a. Yield surface compared to failure surfaces in principal stress space.

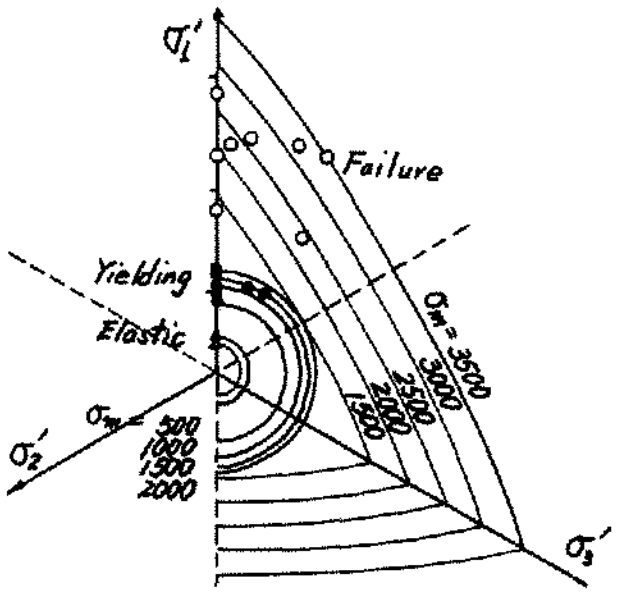

Figure 6b. π-Plane cross sections of yield and failure surfaces.

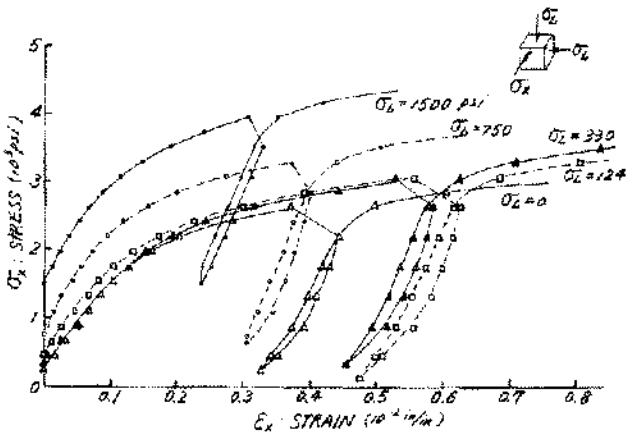

Figure 7a. Conventional stress-strain diagrams of halite.

affected at all. The π-plane cross sections are shown in Figure 6b.

Conventional stress-strain testing fails to indicate the stress state with respect to those critical surfaces of Figures 6a and b. All the test results in the conventional testing appear as diagrams of Figure 7a. If, however, the same experimental results are analyzed in tensor, the condition of the stress state may be identified. One result of the tensor analysis is the Poisson's ratio and stress relation of Figure 7b. Under the brittle deformation, the Poisson's ratio continues to increase, indicating the absence of an elastic state, until the material disintegrates. Under a large confining pressure, the Poisson's ratio changes from a constant elastic value of 0.1 to a constant plastic value of 0.5 and remains at 0.5 with further increase of the applied stress. This indicates the elastic to plastic transition of the

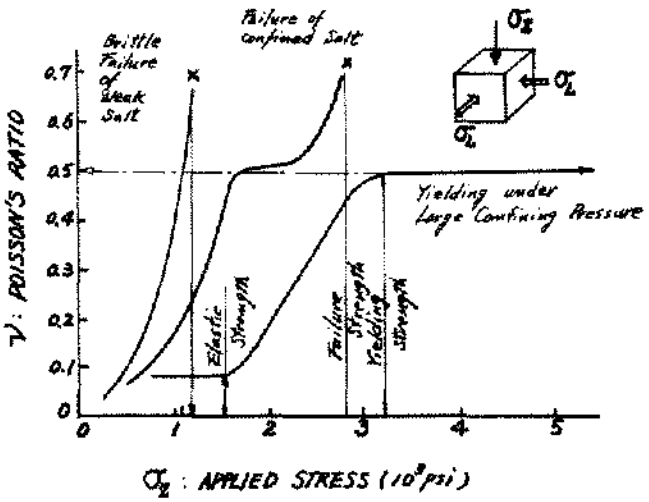

Figure 7b. Stress-Poisson's ratio relation illustrating different deformation mechanisms.

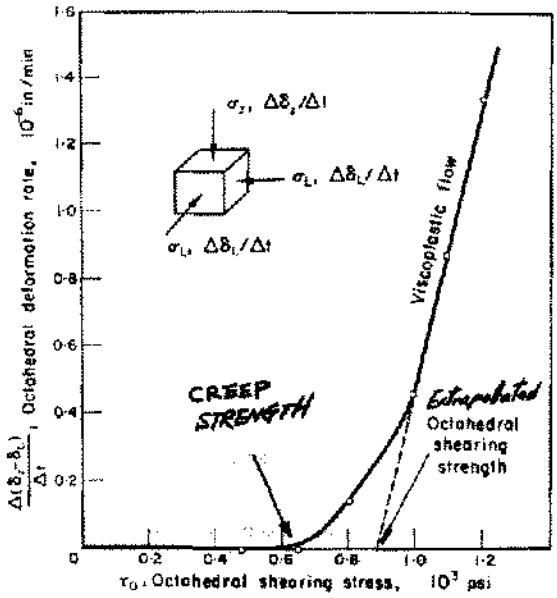

Figure 8a. Octahedral shearing strength of halite determined by creep tenor.

material followed by continuous viscoplastic flow without material failure. As illustrated in Figure 7b, most field conditions fall between the above two extreme cases.

Rock salt specimens always creep whenever they are subjected to a change of the stress state. The creep takes place regardless of the stress state, whether it is inside or outside of the yield surface. However, the creep vanishes within a few weeks if the stress state is inside the yield surface, while the creep continues indefinitely if the stress state is on or outside the yield surface. By using halite, the yield surface was found to be at K_o = 650 psi under a confining pressure equal to or greater than 1,500 psi. Determination of the octahedral shearing strength under the creep is illustrated in Figure 8a. When the stress state is less than the creep strength of K_o = 650 psi, the creep takes place mainly by grain consolidation as shown in Figure 8b. Whenever the stress state exceeds the strength, the creep takes place mainly by molecular dislocation as illustrated in Figure 8c. This difference in the creep is utilized for analyzing the stability of creeping rock media in the laboratory and underground.

LABORATORY ANALYSIS OF SOLUTION CAVITIES

There are three basic factors which determine the behavior and safety of solution cavities created in a deep underground salt formation. They are the tensor properties of the rock salt, the stress field in the formation and the geometry of the cavity in relation to the salt formation. Each factor can be individually determined even in the underground with accuracy sufficient for engineering analysis and design. However, the combination of the three factors is a difficult problem to solve due to the inelastic coupled effects of the properties of the material. Schematic diagrams of long solution cavities in salt domes are shown in Figure 9a.

A laboratory model technique was developed to study the cavity behaviors in relation to these three basic factors and their coupled effects. The objective of the study is to numerically describe the behaviors of solution cavities in the underground by using the constitutive equations of the material. The laboratory model was found to be most useful for the formulation of the cavity behaviors because the three basic factors can be controlled accurately. The standard halite was used to represent the tensor properties of the underground. A hydraulic loading system was developed to regulate the stress field. For the study of the coupled effect of the geometry, a circular thick-walled cylinder was adopted. The behaviors of the cylinder were analyzed by using the constitutive equations and the results compared with the laboratory model behaviors.

According to the results of the theoretical analysis, the plastic zone first appears around the inside boundary r = a when the external pressure

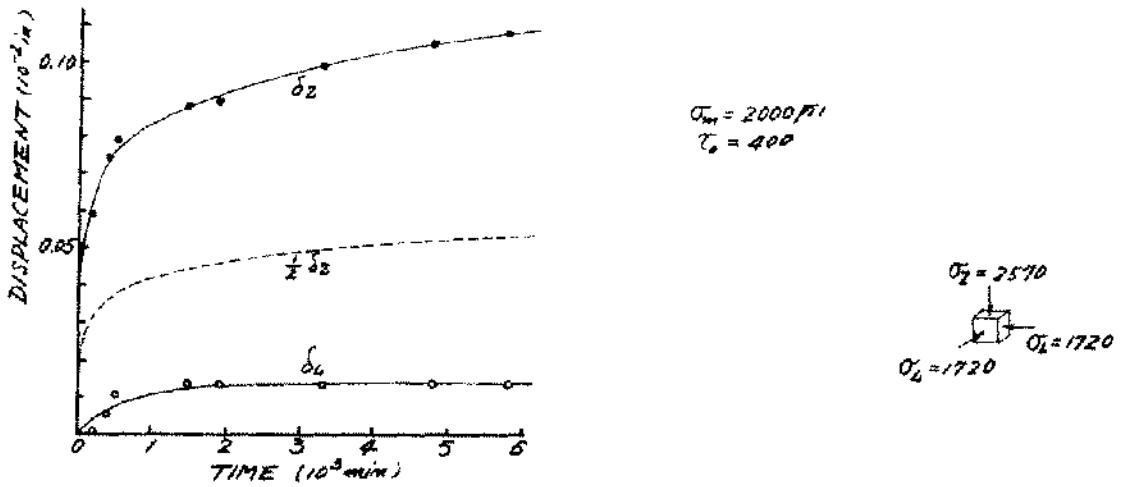

Figure 8b. Viscoelastic creep under octahedral shearing stress less than K_0.

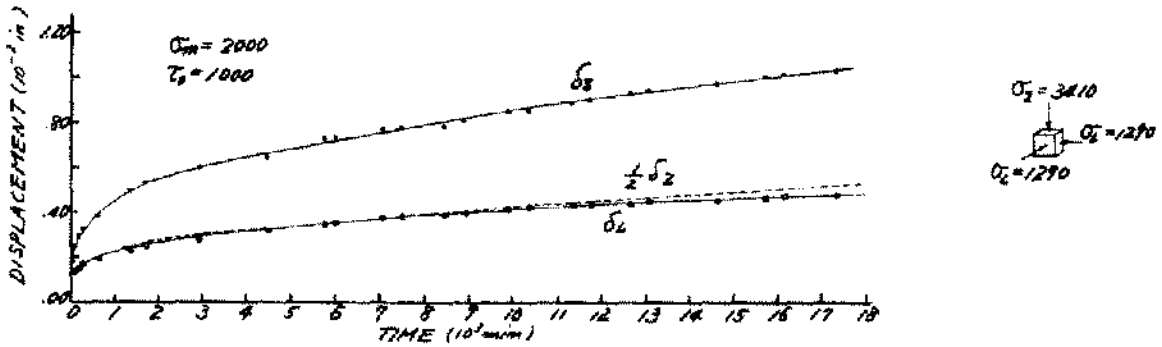

Figure 8c. Viscoplastic creep under octahedral shearing stress greater than K_0.

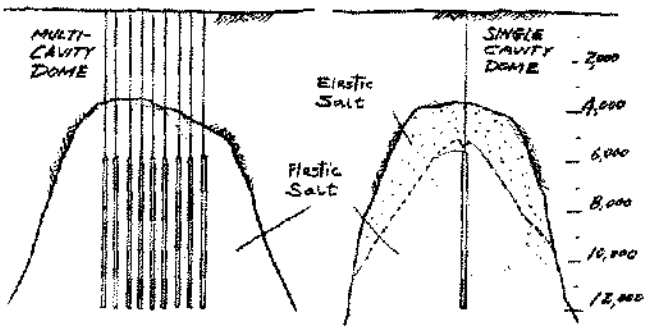

Figure 9a. Comparison of plastic zones around single and multiple solution cavities in salt domes

exceeds a certain value of $P_o = P^*$. The radius of the plastic zone expands outward until it reaches the outside diameter of the cylinder, as illustrated in Figure 9b. Then the whole specimen becomes

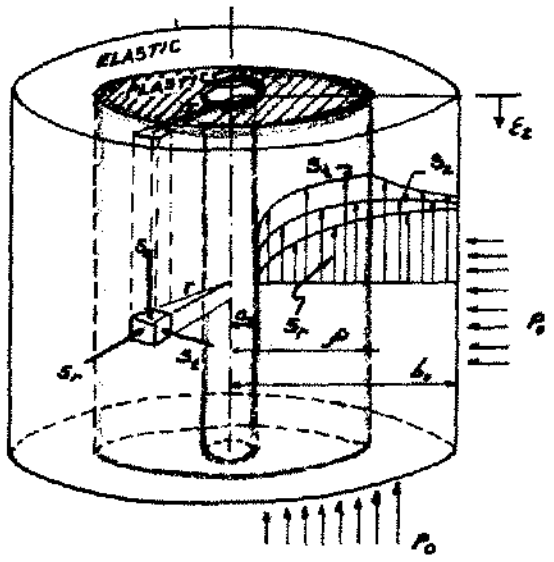

Figure 9b. Laboratory model of single cavity with development of plastic zone.

completely plastic. The behaviors of the laboratory model cavity was found to be quite close to the theoretical prediction.

The creep closure of the model cavity of a thick-walled cylinder tested under the temperature of 250°F is given as an example with respect to the loading time, as shown in Figure 10a. There is no

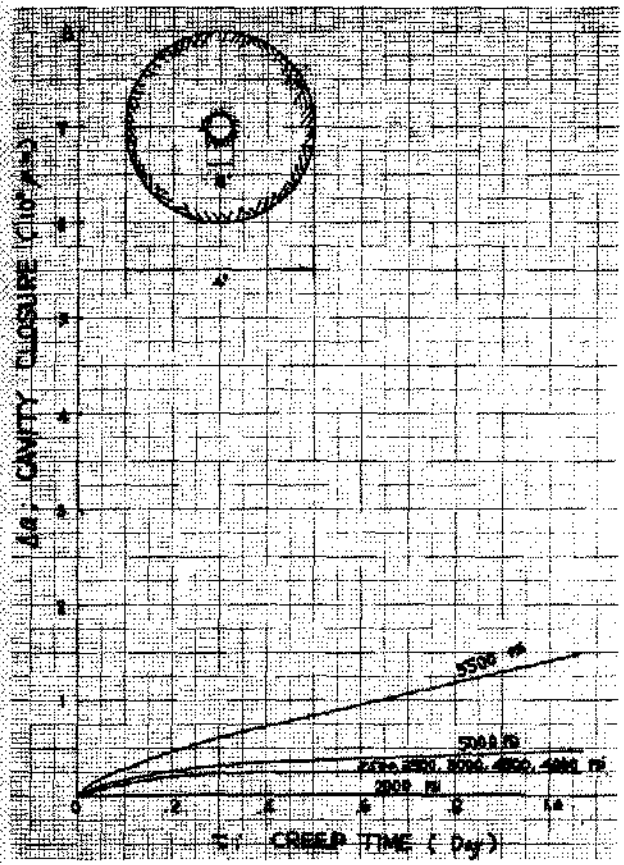

Figure 10a. Single solution cavity model showing viscoelastic point P* = 2,000 psi and viscoplastic point P** = 5,000 psi at 250°F.

appreciable creep deformation for external pressure less than 1,000 psi. With the pressure ranging between 1,000 and 2,700 psi, there is a consistent incremental creep responding to a given incremental pressure increase. This transient creep vanishes within about a half day. The continuous deformation starts whenever the pressure exceeds 2,700 psi. With a further increase of the applied pressure, the viscoplastic creep starts taking place. The viscoplastic creep continues indefinitely with its rate proportional to the amount of pressure exceeding 2,700 psi. The first critical pressure of $P_o = P^* = 1{,}000$ psi is called the "viscoelastic point" at which the model cavity starts deforming viscoelastically. The second critical pressure of $P_o = P^{**} = 2{,}700$ psi is called the "viscoplastic point" at which the model cavity starts deforming viscoplastically. The experimental verification of these two critical pressures may be considered as partial evidence of the validity of the tensor theory of halite. It is this cavity method that was utilized for the determination of the octahedral shearing strength K_o of the halite. The results of the cavity test with respect to the temperature are compared with the results obtained from the direct tensor method as shown in Figure 4c.

The same technique was applied to analyze multicavity behaviors by using a model which consists of four circular holes in an axisymmetric layout, as shown in Figure 10b. The tensor analysis of the four-hole model indicates a similar cavity behavior except for a considerable reduction of the

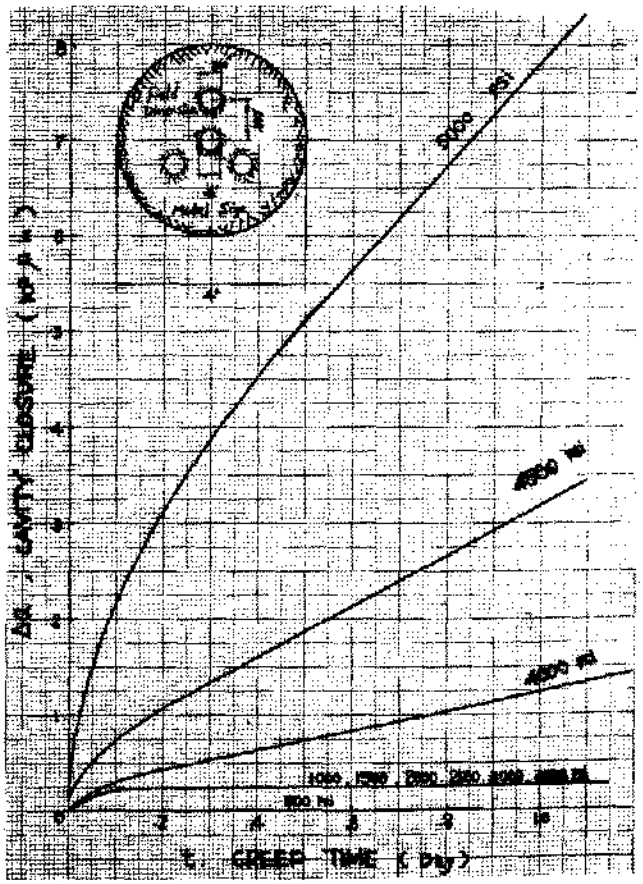

Figure 10b. Multiple solution cavity model showing substantial reduction of viscoelastic and viscoplastic points at 250°F.

two critical pressure points, P* and P**. The results of the model experiments at 150°F also agree with the theoretical prediction as shown in Figure 10c. Both the viscoelastic and viscoplastic points

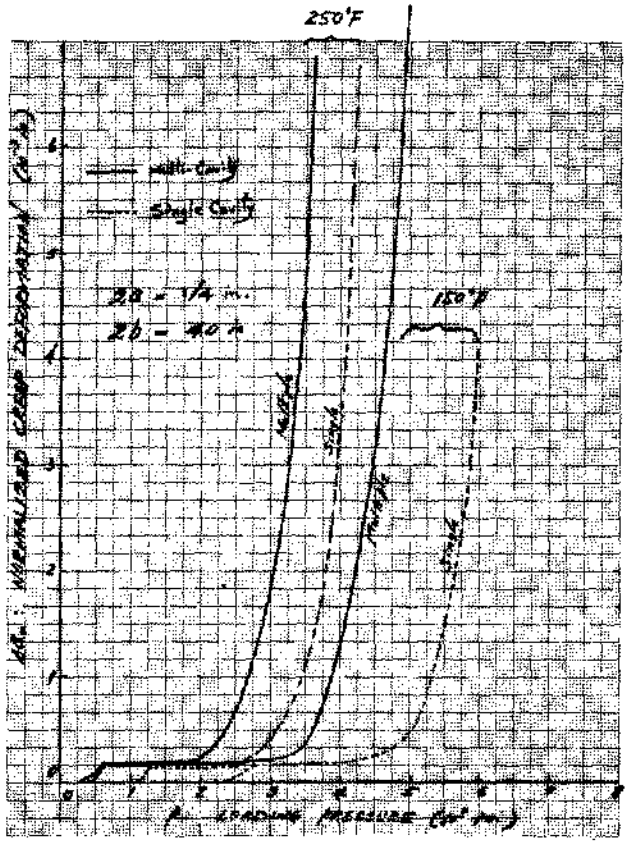

Figure 10c. Comparison of single and multiple cavity model behaviors at two different temperatures.

are significantly reduced by increasing the number of cavities as well as temperature. The parallel nature of the four curves of the diagram proves that a set of multiple cavities behaves like a single cavity with the "equivalent diameter." It also shows how quickly the cavity closes by the viscoplastic flow as predicted by the constitutive equations of the material. Under the viscoplastic flow, the closure data can also be used for determination of the viscoelastic and viscoplastic tensor coefficients. The viscoelastic coefficient analysis is illustrated in Figure 10d. The viscoplastic coefficients were determined under various temperatures, as given in Figure 4d.

The experimental facilities which were used for the laboratory model experiments are shown in Figure 11.

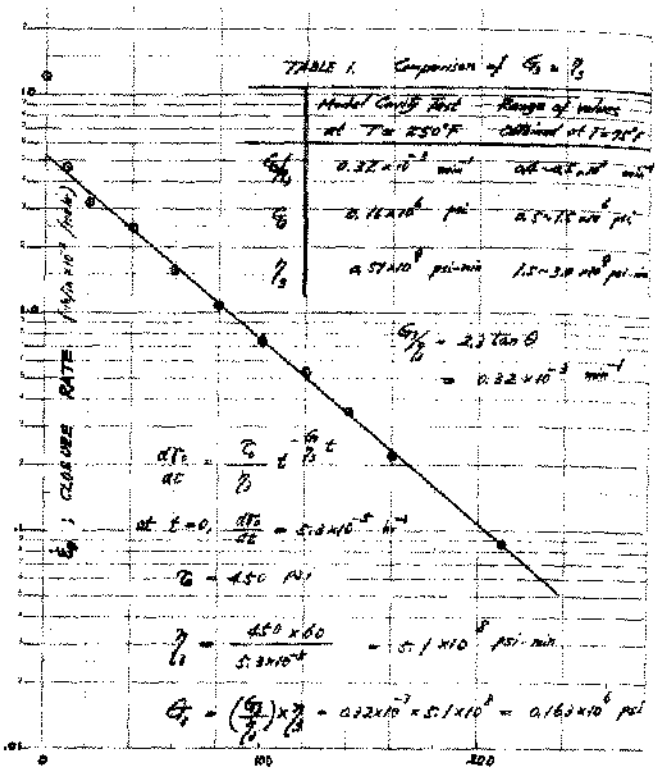

Figure 10d. Determination of viscoelastic coefficients from single cavity model under completely plastic state.

FIELD ANALYSIS OF SOLUTION CAVITIES

The behaviors of solution cavities may be described mathematically by using the constitutive equations of the material. The mathematical theories are derived from the tensor properties of the salt and refined by the laboratory model study. In comparing the creep closures between underground cavities and laboratory model cavities, there is one important difference. In the model cavities, they may be completely closed by increasing the applied pressure. In the underground cavities, there is no complete closure regardless of the magnitude of the earth pressure. The difference is due to the displacement restrictions imposed on the underground cavities from the unlimited extent of ground media. The laboratory models lack such displacement restriction.

The mathematical expression of the underground cavity deformation can be described by the finite element method in relation to the orientation, magnitude of stress field and the material property coefficients, assuming plane strain, homogeneity and isotropy conditions. For a

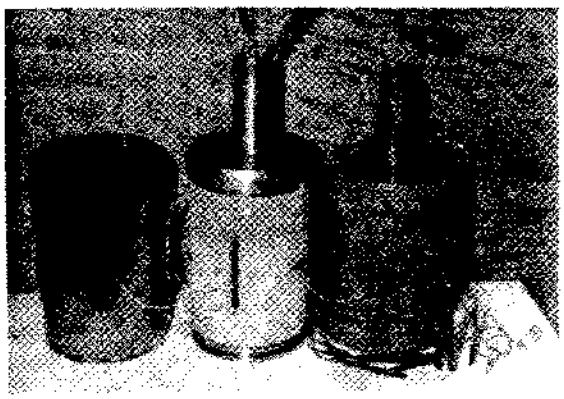

Figure 11a. Typical test specimens with plastic coating and copper jacketing.

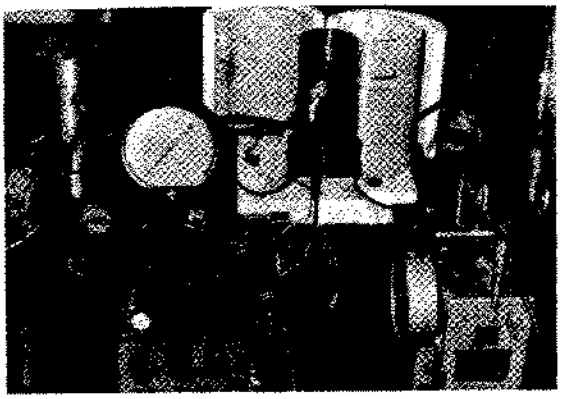

Figure 11b. High pressure testing vessels for room and elevated temperatures.

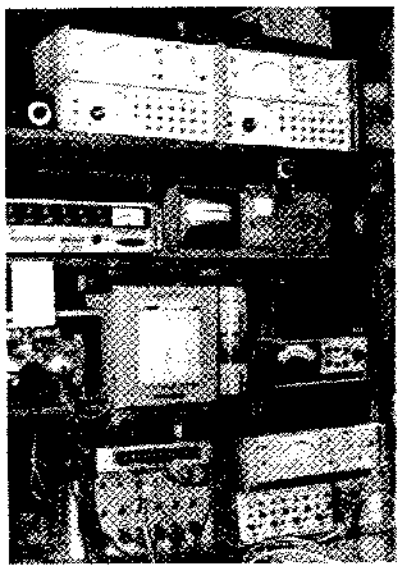

Figure 11c. Automatic control and recording system for cavity model test.

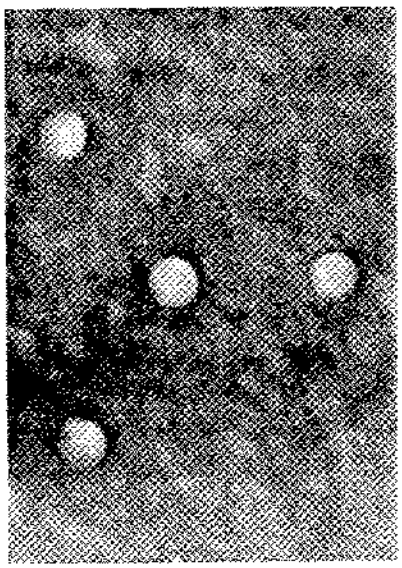

Figure 11d. Thin section of multiple cavity model showing uniform closure after large viscoplastic flow

circular cavity, the equations of the cavity radium change, u, and its time rate, $\dot{u}$, are extremely simplified and expressed by a complex variable method as summarized in the following.

$$u = X\left\{\frac{P_L + P_0}{2}\left(\frac{a^2}{r}\right) + \frac{P_L - P_0}{2}\left(\frac{4a^2}{r} - \frac{a^4}{r^3}\right)\cos 2\theta\right\}$$

$$- Y\left\{\frac{P_L + P_0}{2}\left(\frac{a^2}{r}\right) + \frac{P_L - P_0}{2}\left(\frac{a^4}{r^3}\right)\cos 2\theta\right\}$$

$$\dot{u} = \dot{x}\left\{\frac{P_\perp + Po}{2}\left(\frac{a^2}{r}\right) + \frac{P_\perp - Po}{2}\left(\frac{4a^3}{r} - \frac{a^4}{r^3}\right)\cos 2\theta\right\}$$

$$- \dot{Y}\left\{\frac{P_\perp + Po}{2}\left(\frac{a^2}{r}\right) + \frac{P_\perp - Po}{2}\left(\frac{a^4}{r^3}\right)\cos 2\theta\right\}$$

$$X = \frac{1 - \nu M}{E} + \frac{2 - M}{6G_2}\left(1 - e^{-\frac{G_2}{\eta_2}t}\right) + \frac{1 + M}{3G_2^*}\left(1 - e^{-\frac{G_2^*}{\eta_2^*}t}\right)$$

$$Y = \frac{\nu(1 + M)}{E} + \frac{1 + M}{6G_2}\left(1 - e^{-\frac{G_2}{\eta_2}t}\right) - \frac{1 + M}{3G_2^*}\left(1 - e^{-\frac{G_2^*}{\eta_2^*}t}\right)$$

$$\dot{X} = -\frac{\nu\dot{M}}{E} - \frac{\dot{M}}{6G_2}\left(1 - e^{-\frac{G_2}{\eta_2}t}\right) + \frac{2 - M}{6\eta_2}e^{-\frac{G_2}{\eta_2}t}$$

$$+ \frac{\dot{M}}{3G_2^*}\left(1 - e^{-\frac{G_2^*}{\eta_2^*}t}\right) + \frac{1 + M}{3\eta_2^*}e^{-\frac{G_2^*}{\eta_2^*}t}$$

$$\dot{Y} = \frac{\nu\dot{M}}{E} + \frac{\dot{M}}{6G_2}\left(1 - e^{-\frac{G_2}{\eta_2}t}\right) + \frac{1 + M}{6\eta_2}e^{-\frac{G_2}{\eta_2}t}$$

$$- \frac{\dot{M}}{3G_2^*}\left(1 - e^{-\frac{G_2^*}{\eta_2^*}t}\right) - \frac{1 + M}{3\eta_2^*}e^{-\frac{G_2^*}{\eta_2^*}t}$$

$$M = \frac{\nu + \frac{E}{6G_2}\left(1 - e^{-\frac{G_2}{\eta_2}t}\right) - \frac{E}{3G_2^*}\left(1 - e^{-\frac{G_2^*}{\eta_2^*}t}\right)}{1 + \frac{E}{3G_2}\left(1 - e^{-\frac{G_2}{\eta_2}t}\right) + \frac{E}{3G_2^*}\left(1 - e^{-\frac{G_2^*}{\eta_2^*}t}\right)}$$

$$\dot{M} = \frac{\left\{\left(\frac{E}{6\eta_2}e^{-\frac{G_2}{\eta_2}t} - \frac{E}{3\eta_2^*}e^{-\frac{G_2^*}{\eta_2^*}t}\right)\left[1 + \frac{E}{3G_2}\left(1 - e^{-\frac{G_2}{\eta_2}t}\right) + \frac{E}{3G_2^*}\left(1 - e^{-\frac{G_2^*}{\eta_2^*}t}\right)\right]\right\}}{\left\{- \left[\nu + \frac{E}{6G_2}\left(1 - e^{-\frac{G_2}{\eta_2}t}\right) - \frac{E}{3G_2^*}\left(1 - e^{-\frac{G_2^*}{\eta_2^*}t}\right)\right]\left(\frac{E}{3\eta_2}e^{-\frac{G_2}{\eta_2}t} + \frac{E}{3\eta_2^*}e^{-\frac{G_2^*}{\eta_2^*}t}\right)\right\}}$$

$$\left[1 + \frac{E}{3G_2}\left(1 - e^{-\frac{G_2}{\eta_2}t}\right) + \frac{E}{3G_2^*}\left(1 - e^{-\frac{G_2^*}{\eta_2^*}t}\right)\right]^2$$

The geometry and loading condition are illustrated in Figure 12a. One example of creep closure rate under hydrostatic pressure is shown in Figure 12 by using the tensor coefficients of the standard halite.

The usefulness of the theory was tested in the Prairie evaporite formations in Saskatchewan where various layers of halite, shale, and sylvinite exist. The gamma log taken through the formations at the test site is given in Figure 13. Corresponding

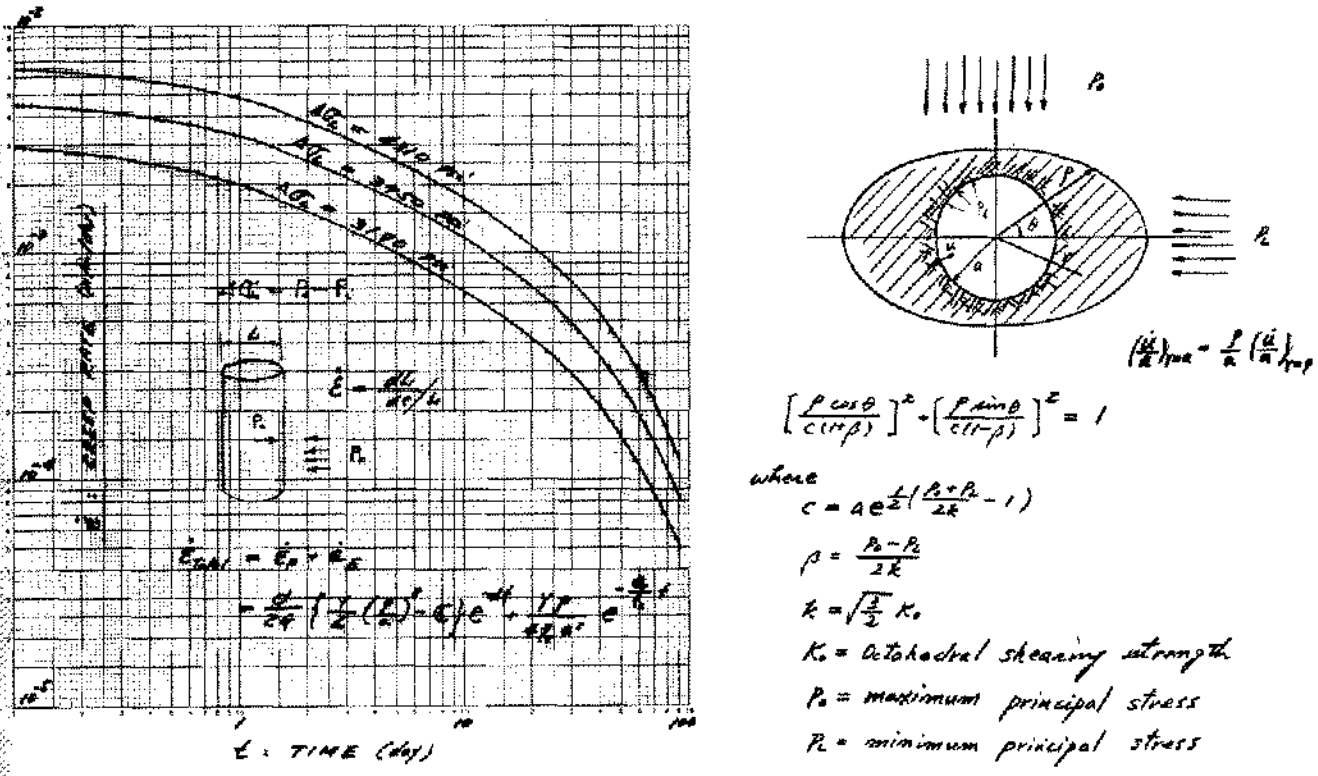

Figure 12. Creep closure rate of cylindrical solution cavity in relation to various pressure conditions.

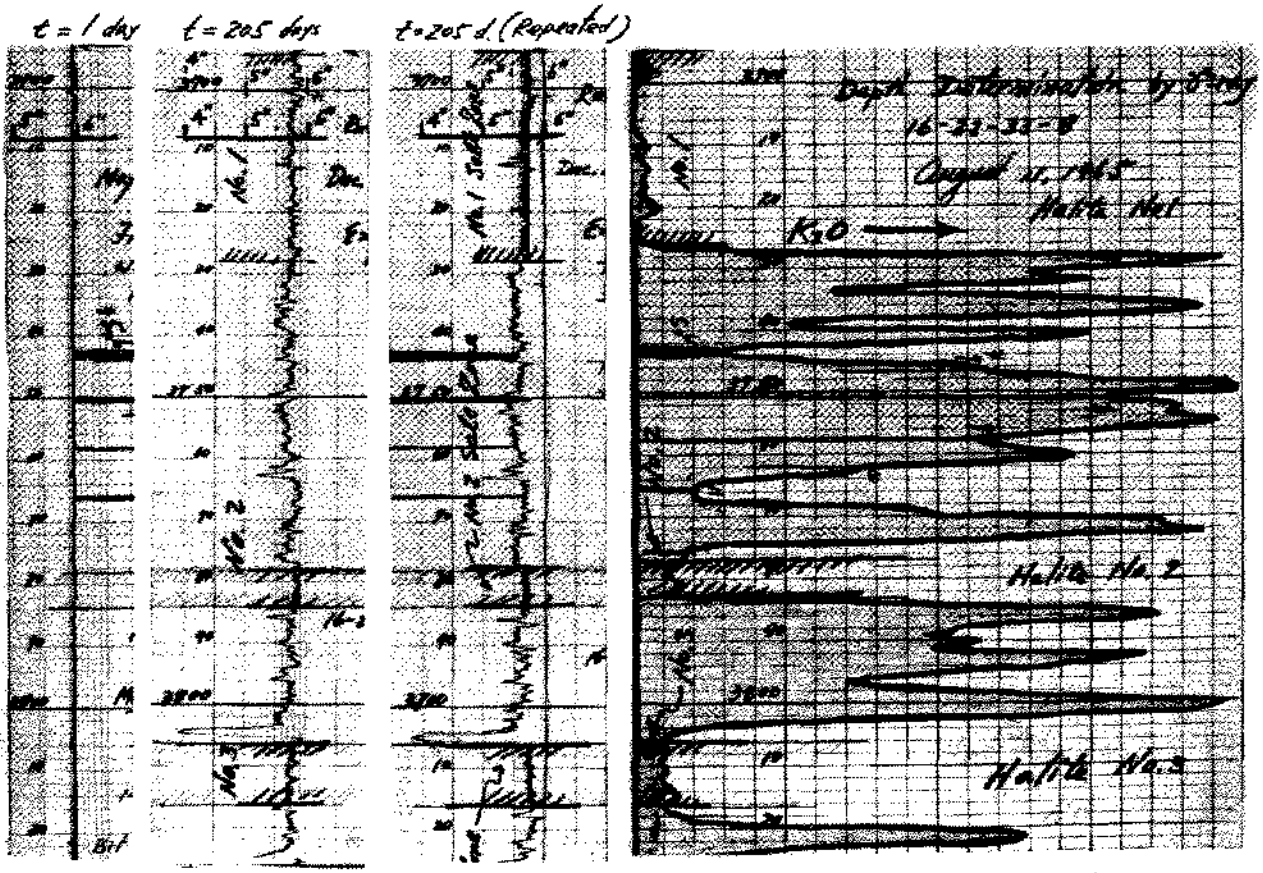

Figure 13. Closure characteristics of borehole relating to various layers of Saskatchewan evaporite formations.

to the gamma logs are three caliper logs of the hole obtained at two different times; at the excavation time and 205 days afterwards. It shows a wide variation in the closure of the 6" borehole ranging from 0.3 to 2.0 in. As demonstrated in the comparison of the logs, the closure of the borehole diameter is directly related to the mineralogical properties of the ground. The closure is fairly uniform at the three halite zones as indicated in the figure. By using the constitutive equations, the average lateral stress field of 4,700 psi was calculated from the constitutive equations by using the tensor coefficients of the standard halite.

This magnitude of the stress was found to be too large for the ground. It was therefore reexamined by installing an electronic borehole creepmeter which recorded the borehole closure continuously as shown in Figure 14. The recording of the closure disclosed a significant irregularity of the curves. Judging from the nature of the irregularity and magnitude of the cavity closure, we assumed that both the viscoelastic creep and probable crystal growth on the exposed surface contributed to the excess closure.

One method of eliminating this growth is to analyze the closure with the cavity filled with a salt saturated non-volatile fluid. Such an example is shown in Figure 15 in which four caliper logs taken at different times are compared. The caliper logs were taken at the 100 foot (10,212' to 10,312') test section of the experimental solution cavity. The results are in good agreement with the theoretical prediction. The stress field can be calculated accurately if the tensor coefficients of the material are determined in the laboratory.

Another method of cavity creep closure measurement is to record the overflow of the filling liquid from the test solution cavity. As the theory indicates, the overflow rate continues to decrease with time due to the establishment of the structural equilibrium around the cavity. A typical overflow characteristic from a test well made in a salt

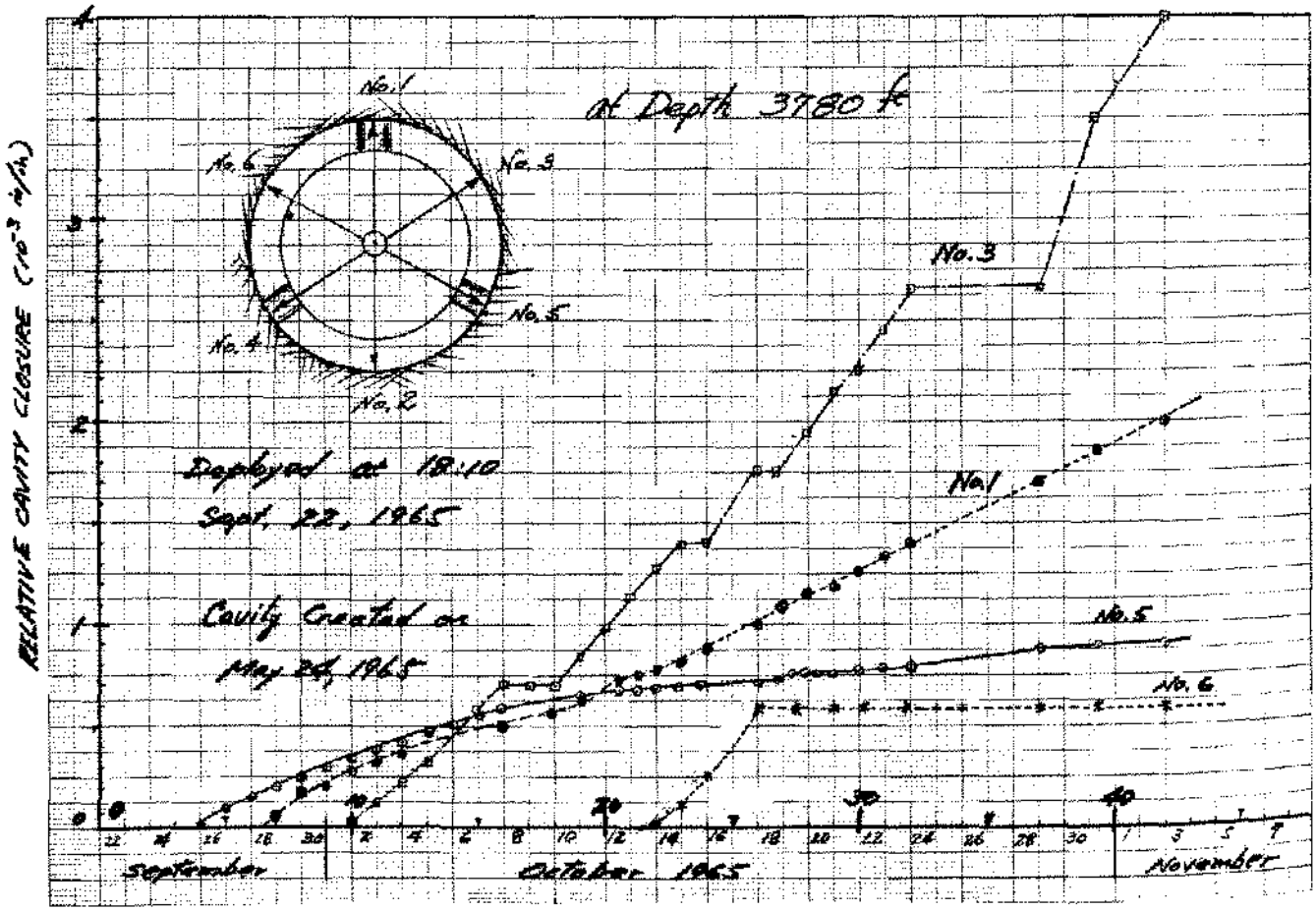

Figure 14. Continuous recording of cavity closure using electronic borehole creepmeter.

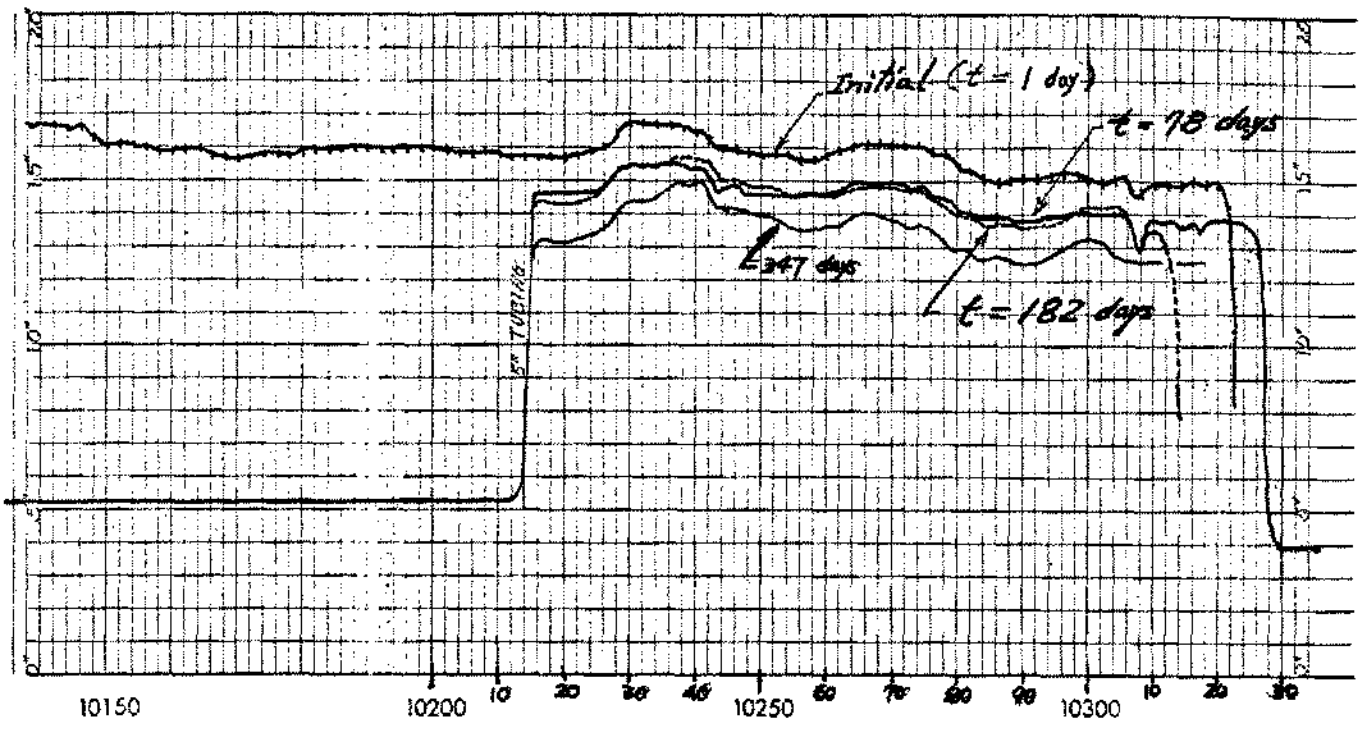

Figure 15. Creep closure of submerged solution cavity analyzed by caliper logs at 100 ft. Test section between 10,212′–10,312′.

dome is illustrated in Figure 16. This method is the simplest one. However, it requires careful casing and sealing of the test well. A slight inflow of ground water may easily upset the test result. It is therefore recommended to use at least one caliper logging for a cross-examination of the overflow measurements.

LABORATORY ANALYSIS OF CONVENTIONAL MINES

The three basic factors in determining the behaviors and safety of underground mine structures are the tensor properties of the rock, stress field of the ground and geometry of the mine structures. The method of determining the tensor properties has been discussed extensively in Chapter II. In laboratory testing, the application of the three-dimensional stress for investigating mine structures is the most important requirement. The effect of the three-dimensional stress field is illustrated by using the three-dimensional testing devices. The nature of the rooms and pillars of conventional mines was studied and the results are summarized in the following.

The effect of the stress field was studied by testing the creep closure of a circular hole under two

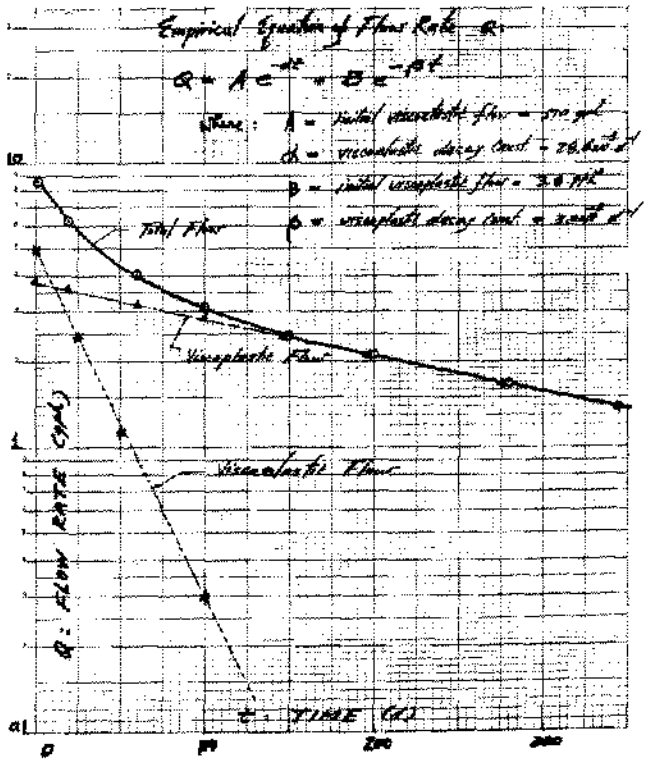

Figure 16. Characteristic curve of overflow rate from experimental solution cavity in deep salt dome.

different types of loading. One type of loading is triaxial in which the three principal stresses are equal as $P_x = P_y = P_z$. The other type is a biaxial one in which the two principal stresses are equal but the third one is zero as $P_x = P_y$, $P_z = 0$. Under each type of loading, the stress was increased in steps, as illustrated in Figure 17. A circular cavity was drilled after the 5" × 5" × 5" specimen was preloaded, then the behaviors of both the cavity and the cubic specimen were observed. As shown in Figure 17, the cavity closure under the triaxial loading is much greater than that under biaxial loading.

A cavity created in a medium under an elastic stress state always reaches a stable equilibrium after a certain creep deformation, as discussed in Chapter IV. When a cavity is created in a medium under the viscoplastic stress state, the cavity will never reach a stable equilibrium. Instead, the cavity continues to deform linearly as shown in Figure 18.

Previous experience in the stress-strain of a structure has a significant effect only for a limited period following the loading. This effect by the experience is demonstrated by using cavity closure test. Two identical cubic specimens with a circular hole were loaded to P_c = 4,000 psi in two different ways, as illustrated in Figure 19. It shows that the difference in the experience vanishes with increase of the creep time. The creep closure patterns under various loading pressures were obtained by using the triaxial loading device, as shown in Figure 20. The device creates a passive stress in the direction of the cavity due to the restriction of the axial expansion. The axial stress is determined by the transition characteristics of the material.

The three-dimensional testing stand which is used for studying the opening closure in a uniform stress field is shown in Figure 21. The test openings are drilled through the loading plate. The partially triaxial loading device is shown in Figure 22. A 5" cubic specimen placed in the device is loaded externally in the two principal stress directions. A passive stress is produced by the confinement in the third principal stress direction. The confining plate is exchangeable with two different types, one with

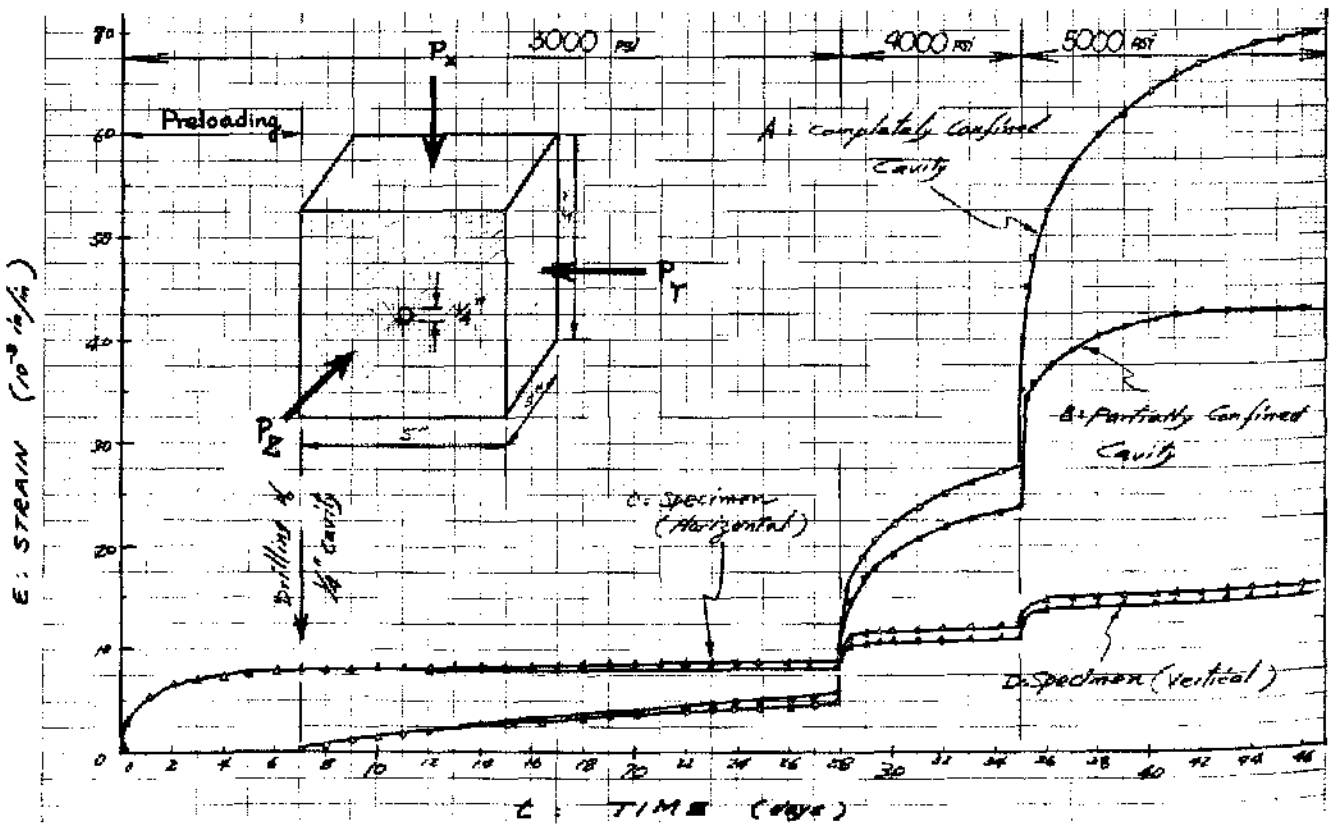

Figure 17. Comparison of biaxial and triaxial loading effects upon creep closure of circular cavity.

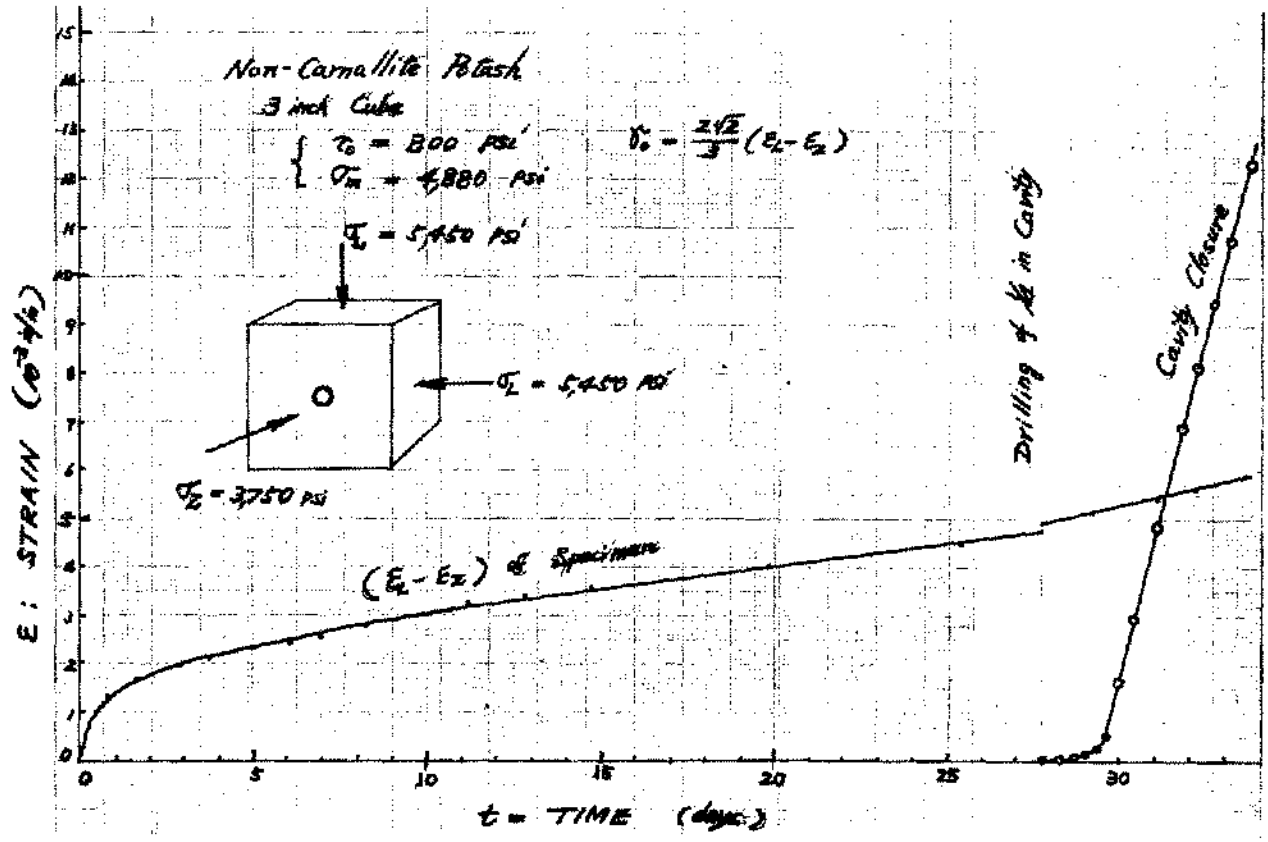

Figure 18. Continuous linear closure of circular cavity drilled through halite under viscoplastic state.

drill holes (one or more) and the other with a large photostress observation window as shown in Figure 22.

The geometry effect can be studied by using either the complex variable method or a finite element method. For studying the general effect of room width for a given excavation height, the complex variable method can be applied effectively. However, the finite element method is more useful for evaluating the effects from specific layers of clay seams which exist in and around the ore body. A specific finite element program is required for every specific geometry and nature of the clay seams.

In studying the general characteristics of the room span effect, the complex variable method is most useful. The expression of stress distribution around an opening with various widths is obtained with respect to the boundary conditions and stress field by using the method. The result of the analysis can be used for evaluating the laboratory model and finite element program.

One example of the solutions from the equations is illustrated in Figures 23a and 23b. The stress distribution shows the retreat of the stress arch deeper into the roof with the increase of the room width. The retreat is accompanied by the spread of the stress arch and reduction of the shear strain gradient. It should also be noted that the stress distribution patterns change drastically with the widening of the room width.

The above theoretical results of the room behaviors were examined by using the photostress analysis which enables us to observe strains in actual rock specimens under large deformations, including both the elastic and inelastic strains. The stress distribution pattern change by the widening of the room width is demonstrated by the four pictures of Figure 25. It is apparent that the nature of the strain distribution is in agreement with the theoretical results. A similar wide-room model study is needed under a triaxial loading condition because the photostress analysis is by necessity in two dimensions. One typical three-dimensional model test is illustrated in Figure 2.

The photostress model technique is useful also in

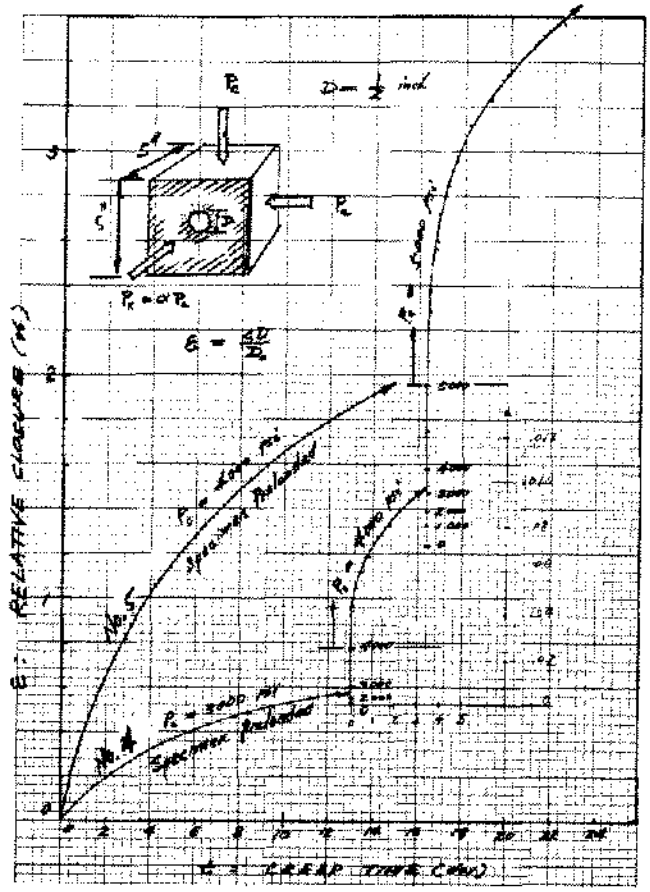

Figure 19. Effect of previous stress-strain experience upon behavior of circular opening.

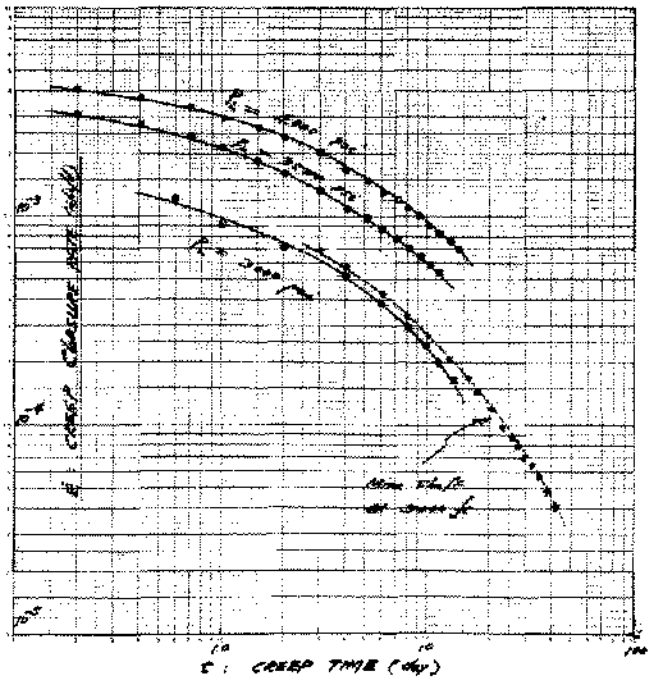

Figure 20. Basic pattern of creep closure rate of circular opening.

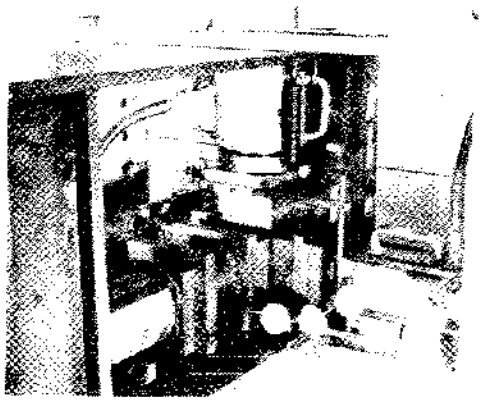

Figure 21. Three-dimensional creep testing stand for studying cavity closure in uniform stress field.

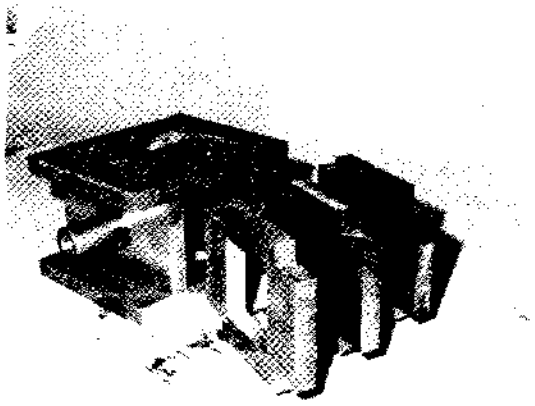

Figure 22. Partially triaxial loading device with two principal stresses externally applied and one internal confinement.

studying underground pillar behaviors. The time-dependent behavior of a pillar created between two entries which are driven at different times is shown in Figure 26a. The photograph shows the non-uniform deformation of the pillar. Another experimental result given in Figure 26b illustrates the behaviors of narrow pillars made between a number of narrow entries. It demonstrates the mechanism of the narrow yielding pillars which can withstand extremely large overburden pressure compared to the uniaxial strength of the material.

FIELD ANALYSIS OF MINE STRUCTURES

In the field analysis of mine structures, the three basic factors of stress field, rock properties and mine geometry should be considered, as similar to the laboratory analysis. The stress field in any salt

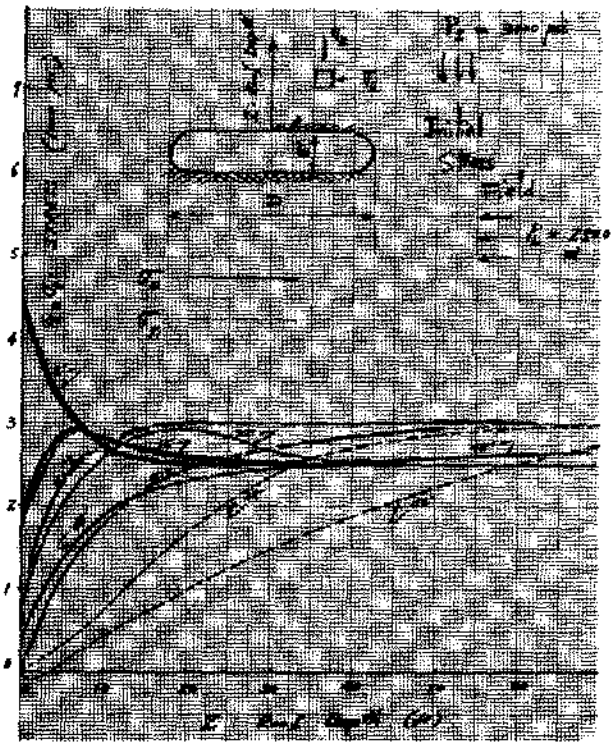

Figure 23a. Effect of room width upon stress distribution above roof center.

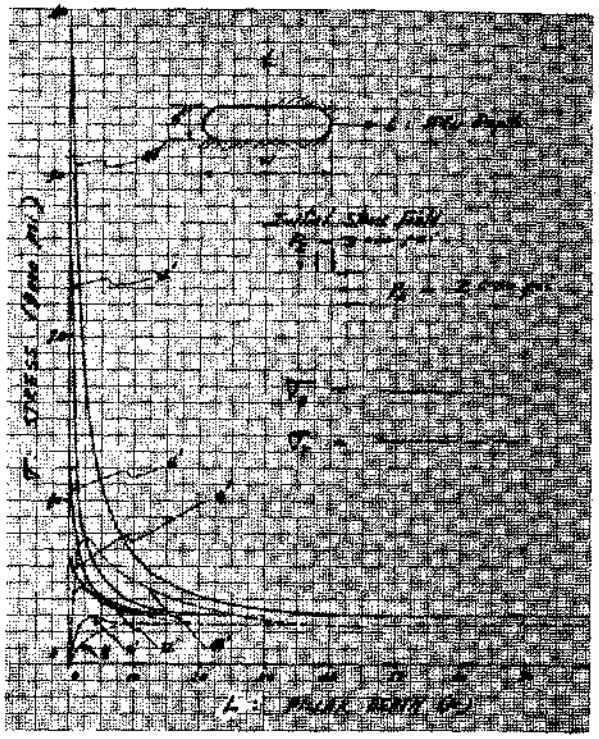

Figure 23b. Effect of room width on stress distribution in pillar.

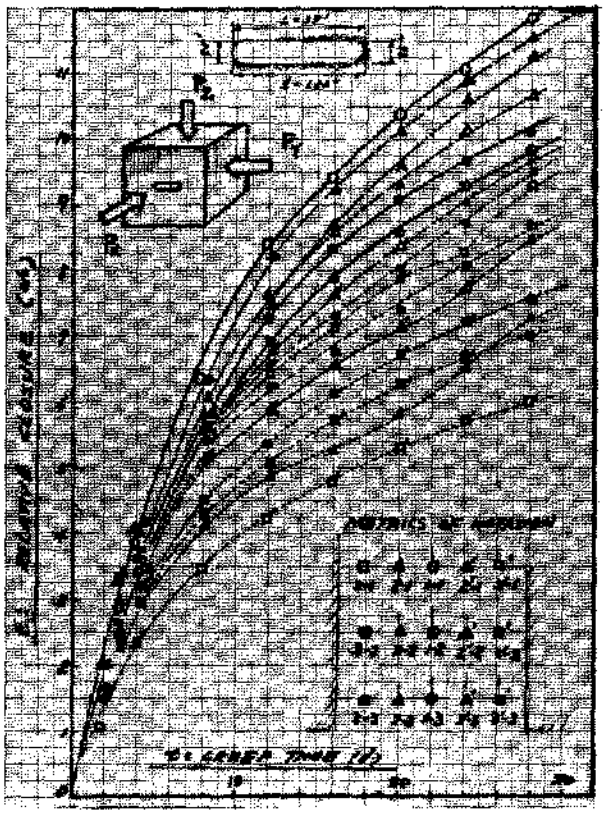

Figure 24. Three-dimensional model testing of wide room to supplement photostress analysis.

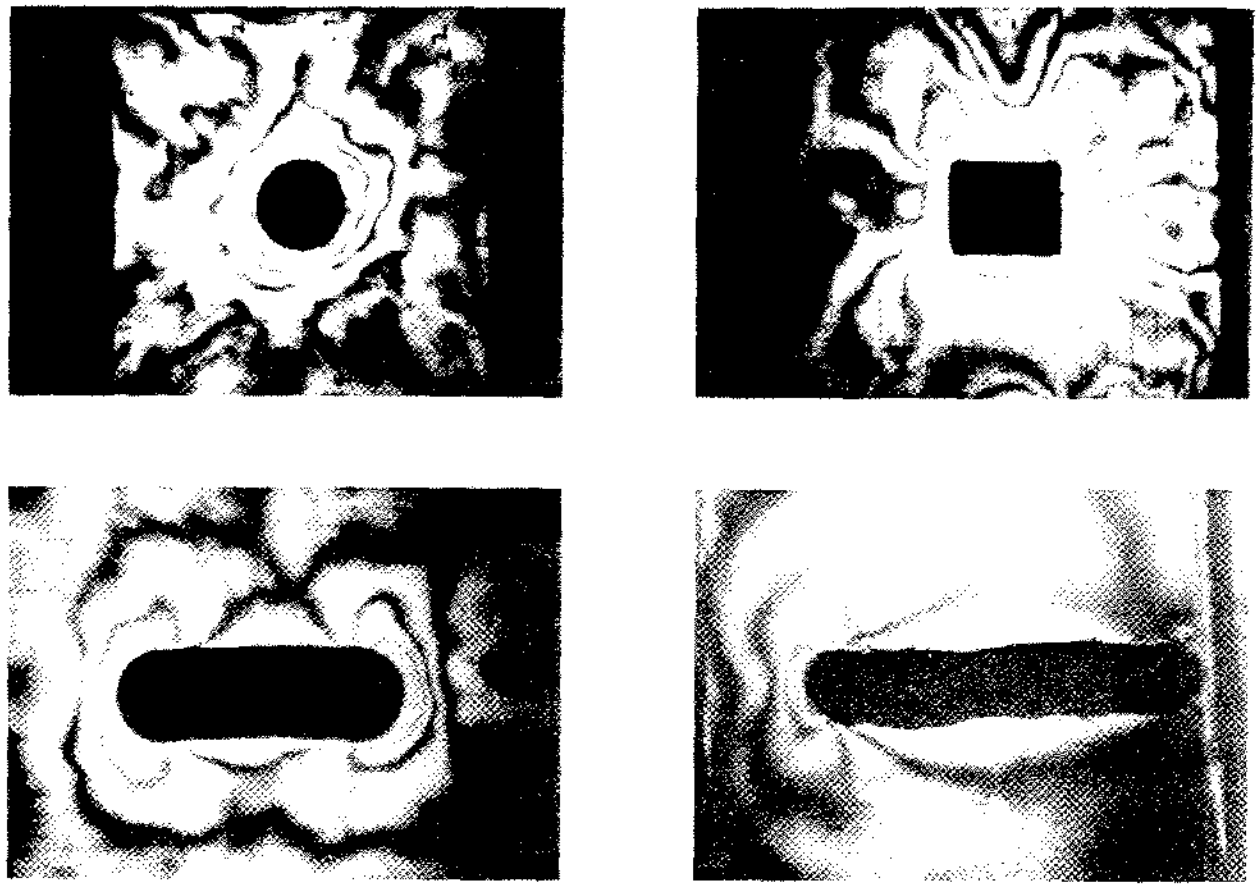

Figure 25. Photostress pictures showing effect of room width on shear-strain distribution around mine opening using halite specimens.

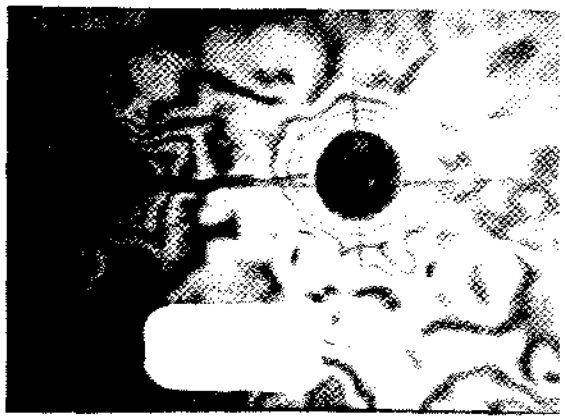

Figure 26a. Irregular deformation of pillar between two entries made at different times.

Figure 26b. Behaviors of narrow yielding pillars under very large earth pressure.

formation is usually not hydrostatic. Therefore it is important to know the exact stress field, particularly for the numerical analysis of mine design. A reliable stress field determination method was developed by using the Borehole Creepmeter which is described in the next chapter. In this chapter, the methods for analyzing the combined effects of rock properties and geometry in the underground are described.

Since the rock properties and stress field are natural conditions for a given mine, it is the mine geometry that we can artificially manipulate in order to design the most economical and safe mine. Therefore, all mine behaviors should be analyzed in relation to the geometry. There are two basic methods for the mine analysis; namely passive creep and active loading methods.

Creep deformation of a mine opening can be analyzed by measuring the displacement distribution around the structure. A typical creep station of a mine opening is shown in Figure 27. A long-term observation of the creep always yields information most useful for evaluating the room safety. An example of a long-term mine entry analysis is shown in Figure 28 in which the room closure at three different locations in the entry is compared. The rapid decline of the creep rate at the intersection Station B compared to the room center Station C indicates that the present width is not wide enough and therefore should be enlarged.

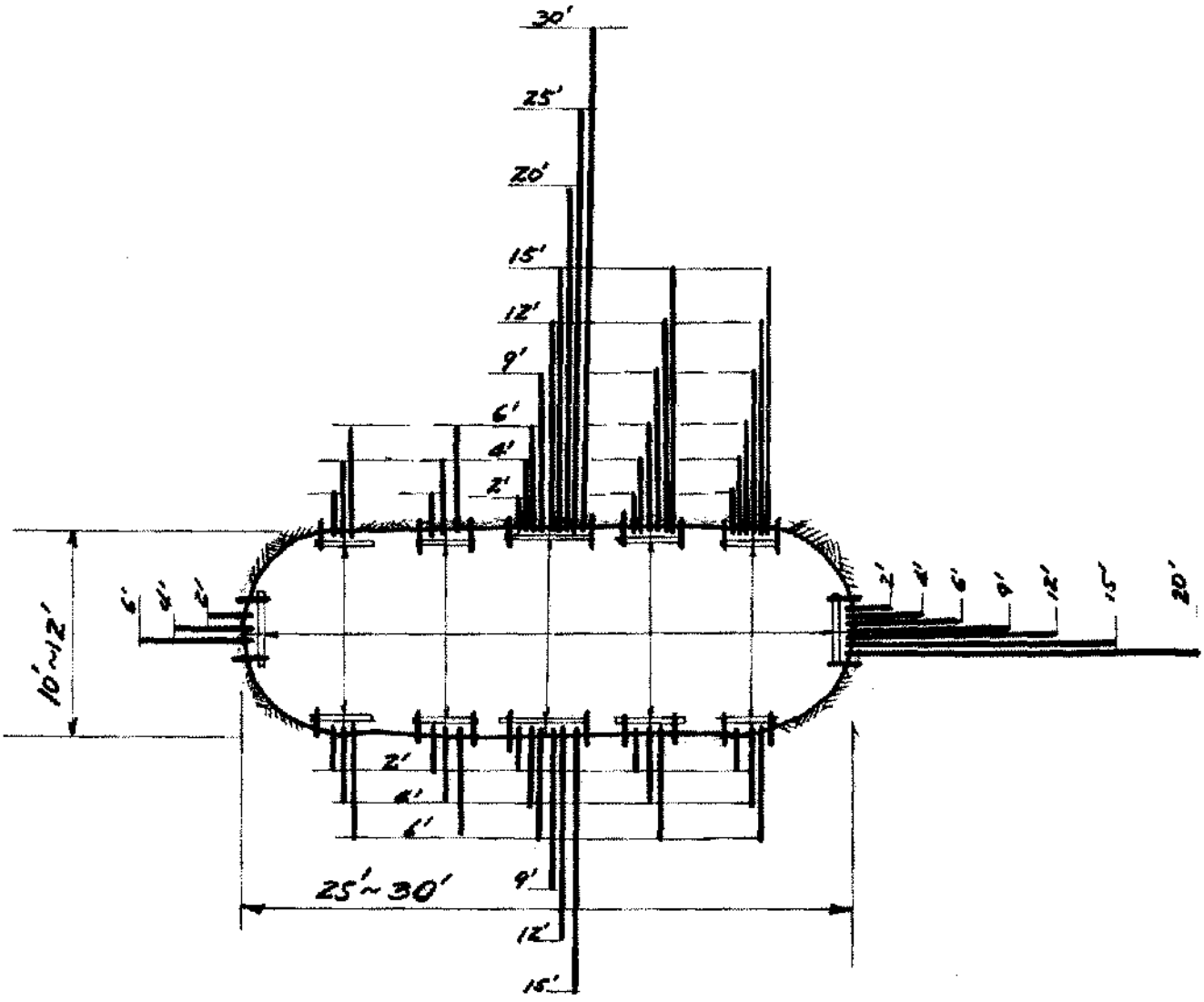

Figure 27. Design example of permanent reference creep station.

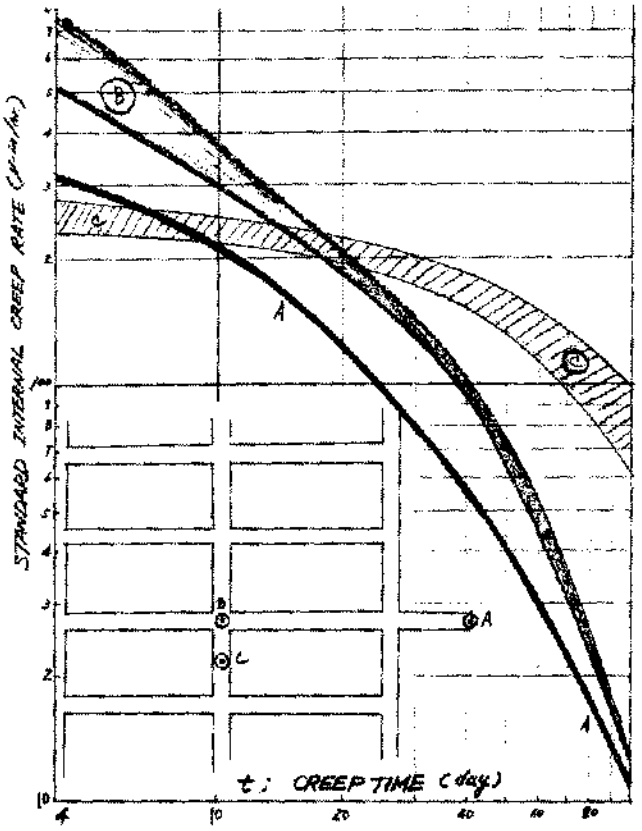

Figure 28. Characteristic creep curves indicating room safety condition in main entry system.

A portable electronic instrument called the Serata Microanalyzer is used for immediate detection of the room closure characteristics. The use of the Microanalyzer is illustrated in Figure 29. Without hydraulic loading, the Microanalyzer records six creep deformations simultaneously. In a few hours of recording, the structural characteristics of a given area may be ascertained. In general, there are two different types of mine roof which are detected by the Microanalyzer, as illustrated in Figure 30.

The Microanalyzer can also be used for the active loading analysis. The deformation responses to an applied load by jacking indicate the conditions of the room. A typical example of loading response of a deteriorating room is shown in Figure 31. The contrast of the load displacement diagrams between competent and deteriorating rooms is demonstrated in Figure 32. In Figure 33, the displacement response profiles along the room centerline are compared between competent and deteriorating rooms. The most important advantage of the active Microanalyzer test is its speed as the active test at one location can be done in less than one hour. Therefore, a large area can be analyzed by the systematic use of the Microanalyzer.

It has been shown by the Microanalyzer study that the safety conditions of any opening can be most accurately assessed by creep analysis of roof

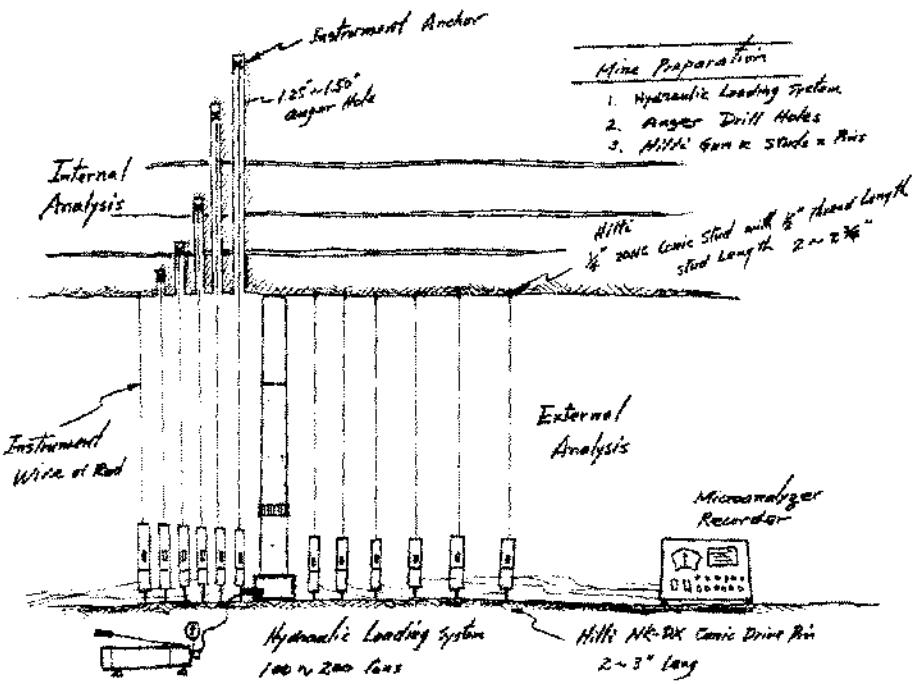

Figure 29. Application of microanalyzer for mine structure analysis.

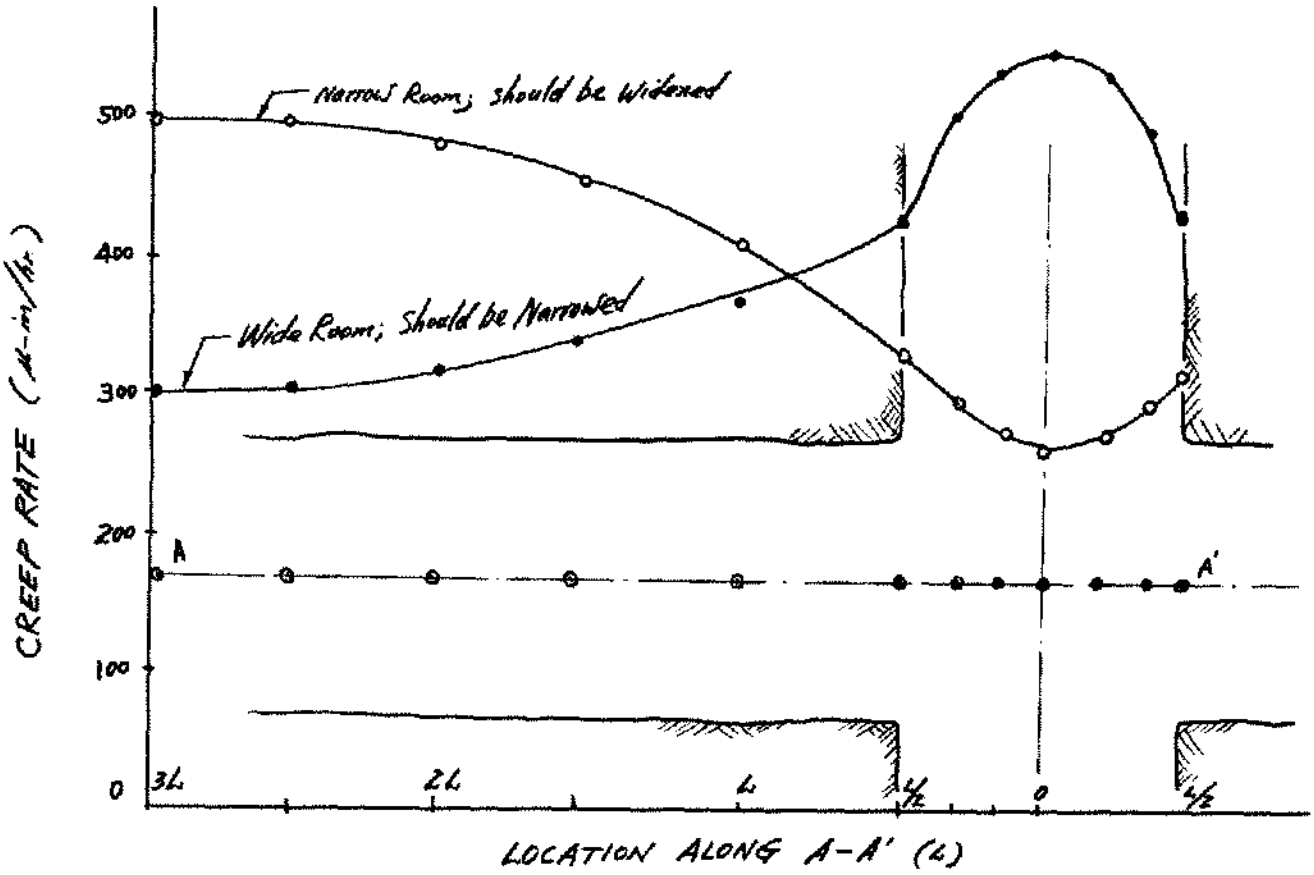

Figure 30. Creep rate distribution patterns reflecting effect of room width.

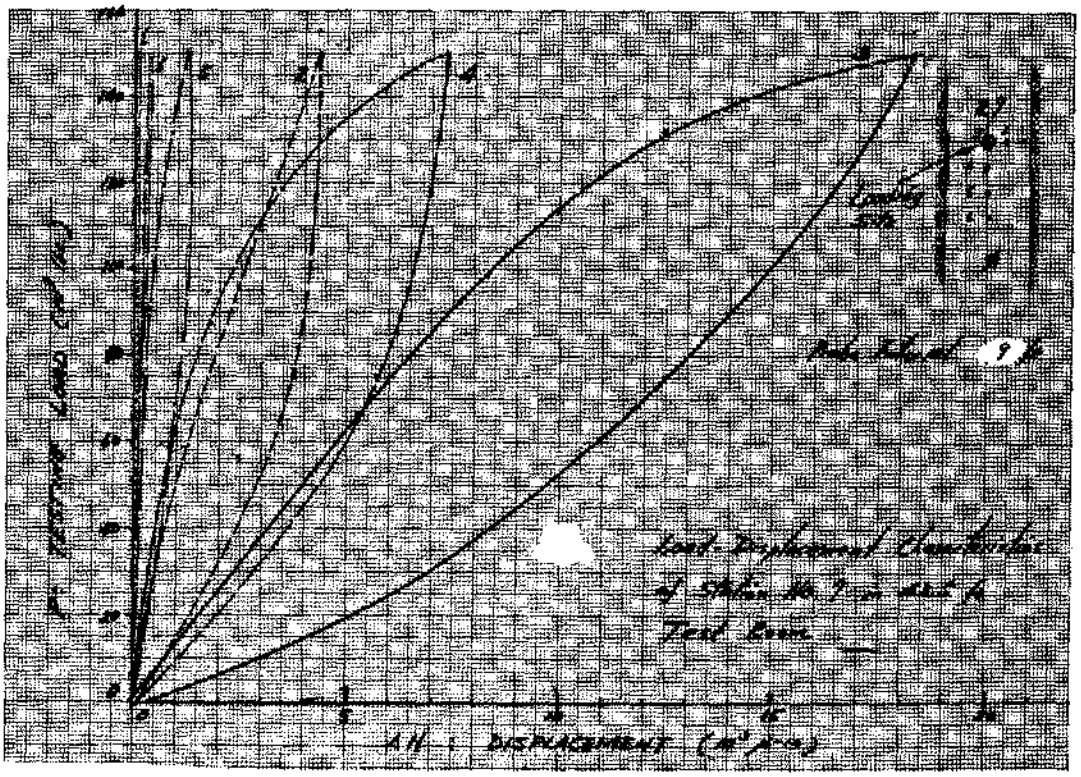

Figure 31. Load-displacement characteristics of deteriorating room.

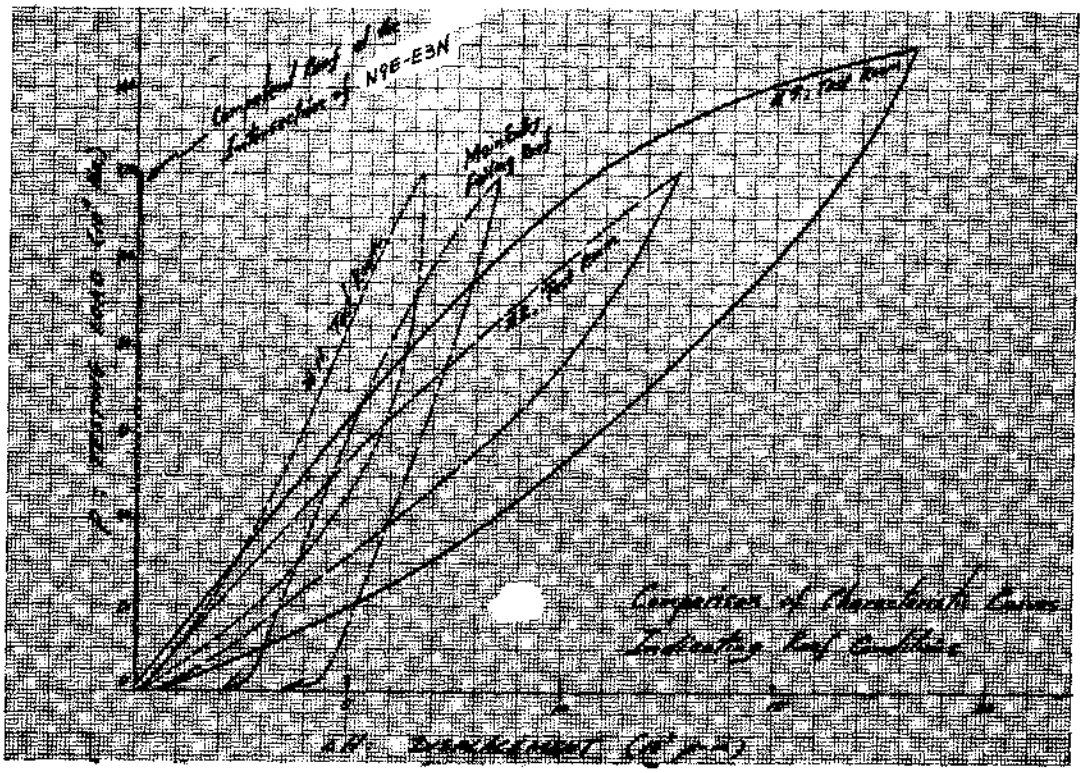

Figure 32. Comparison of load-deformation diagrams between competent and deteriorating rooms.

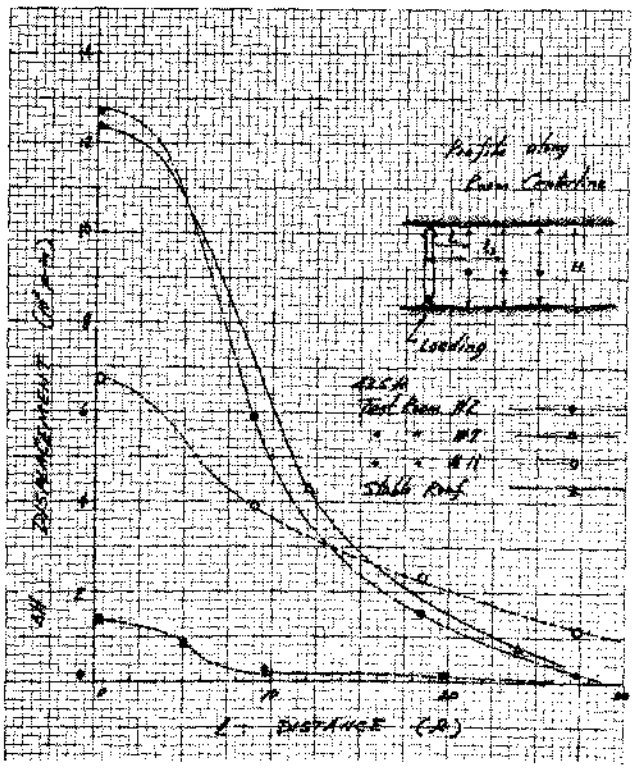

Figure 33. Comparison of displacement profile along room centerline between competent and deteriorating rooms.

media. Individual mines have different rock mechanics properties of their roofs which have specific creep characteristics. However, regardless of the complexity of the roof properties, the creep characteristics of the roof are found to be the most accurate and reliable reference for safety.

It is this characteristic that the Microanalyzer measures in order to detect the roof stability quickly. Further use of the Microanalyzer for an anchor bolt study is illustrated in Figures 34 and 35. The probes and recorder of the Microanalyzer are shown in Figure 36.

DETERMINATION OF UNDERGROUND STRESS FIELD

A new method of determining the underground stress field was developed based on the tensor properties of rocks. A special borehole instrument called the "Borehole Creepmeter" was devised for this purpose. The Borehole Creepmeter measures the creep rate distribution around a borehole in axial and radial directions. The creep rate distribution as a function of time is then converted to the initial stress field by using the constitutive equations of the material.

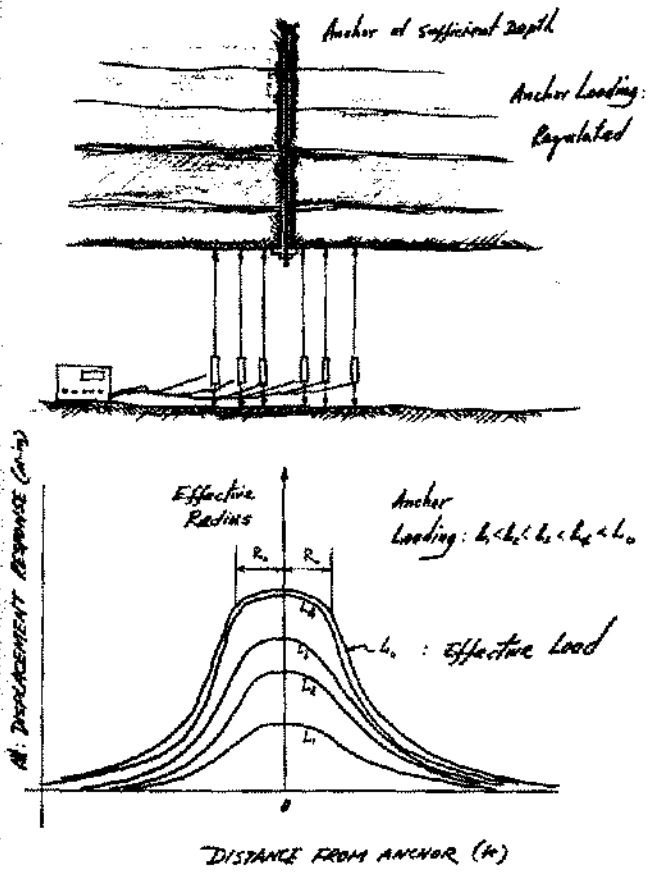

Figure 34. Determination of effective radius and effective load of anchor bolt using microanalyzer.

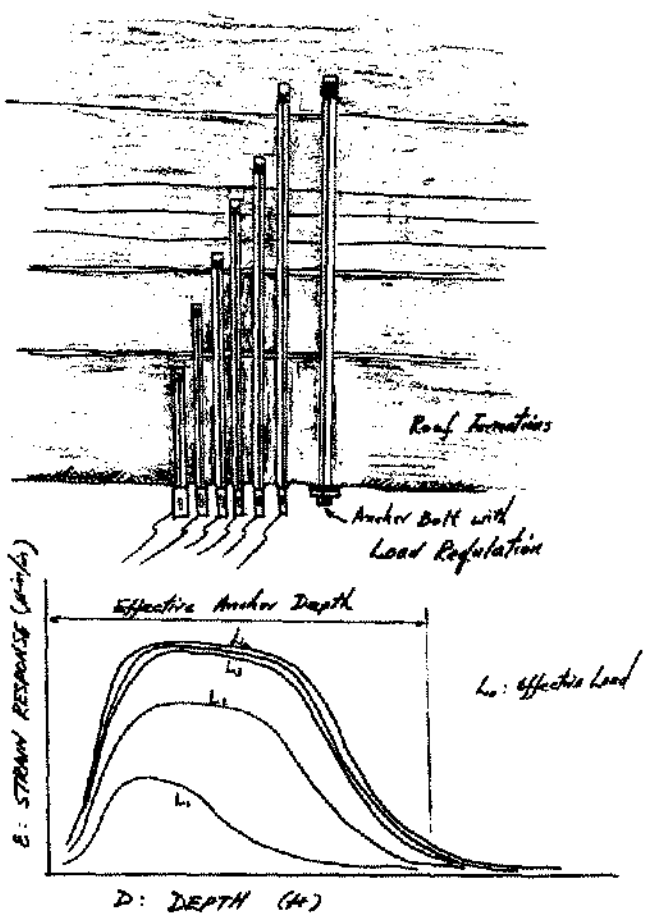

Figure 35. Determination of effective depth and effective load of anchor bolt using microanalyzer.

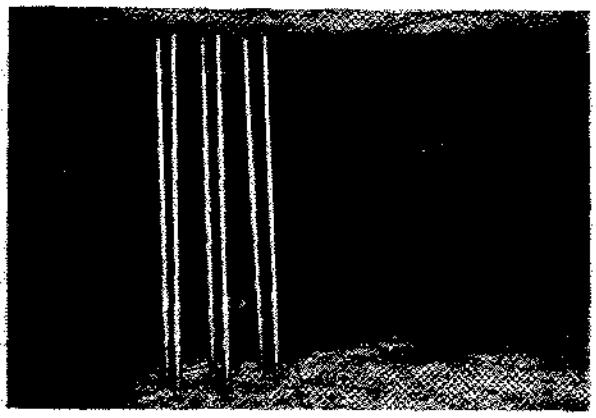

Figure 36a. Six probes of microanalyzer capable of quick installation and high resolution.

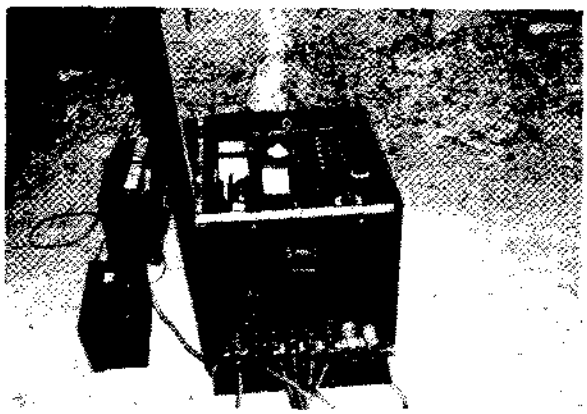

Figure 36b. Portable microanalyzer recorder operated by battery.

The Borehole Creepmeter consists of a number of interchangeable units such as radial probe, axial probe, rotator, rotor, anchor and centralizer as illustrated in Figure 37. The radial probe measures diameter change while the axial probe measures displacement in the direction of the borehole. The anchor fixes the instrument at two separate points for measuring the axial displacement. The rotator and rotor are capable of setting the radial probe at any radial direction in the borehole.

An eddy-current type transducer was adopted for measuring the displacement. The transducer has the advantage of great stability with high resolution.

One of the field test setups is shown in Figure 38. Three Borehole Creepmeters are placed around the test room, two in the roof and one in the wall.

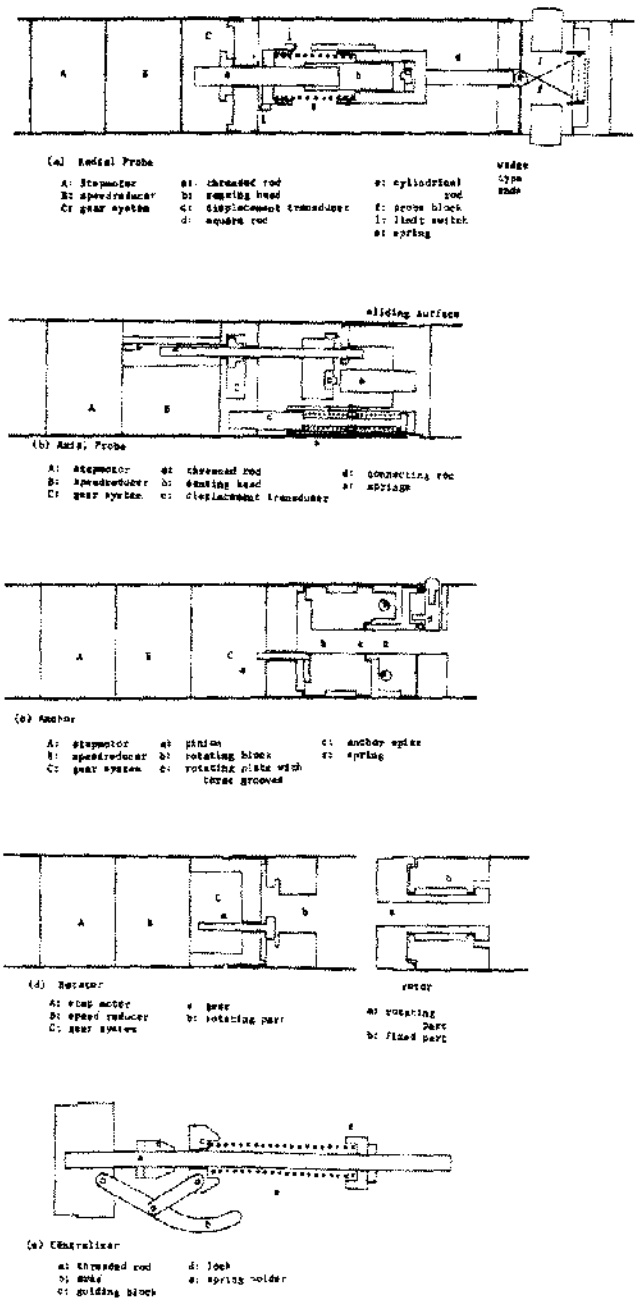

Figure 37. Schematic diagram of components of borehole creepmeter.

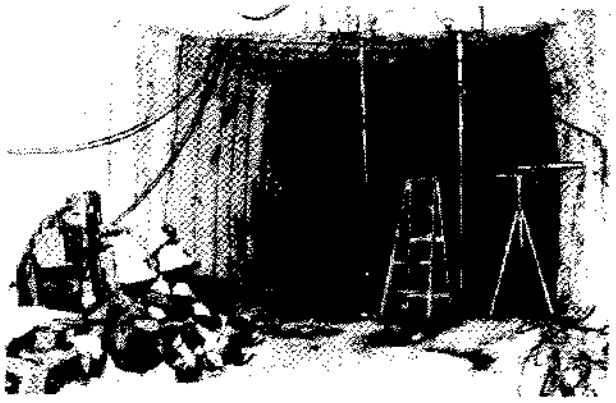

Figure 38. Test site for stress field determination using borehole creepmeter.

The stress field determination made at the Allan Potash Mines, Saskatchewan, Canada is summarized as an example. The measurements were taken at the depth of 3,400 feet, in the Prairie Evaporite formation of the mine.

Four test holes were used for the stress field determination; two horizontal holes in the two mutually perpendicular directions at the north end of North Entry No. 1, and two vertical holes in West Entry. The location of the test holes is shown in Figure 39.

The lateral stress was found to be in the following range from the creep measurements made in Test Hole Nos. 1 and 2, assuming the overburden pressure to be 3,400 psi:

$$0.69\ P_o < P_L < 0.77\ P_o$$

$$2{,}350\ \text{psi} < P_L < 2{,}620\ \text{psi}$$

The stress field in the horizontal plane was measured once more in Test Hole No. 5. A similar attempt in the center hole (No. 6) failed completely because of the continual movement of the immediate roof formations which were in the process of falling. The continuous sliding among the separated slabs of the roof produced a microseismic effect which upset the creep measurement in the hole.

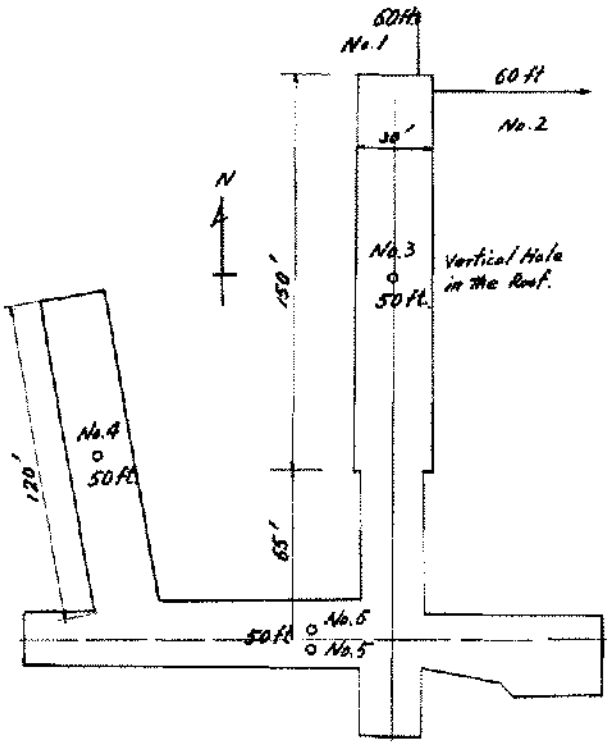

Figure 39. Location of test holes used for stress field determination at Allan Potash Mines, Saskatchewan, Canada.

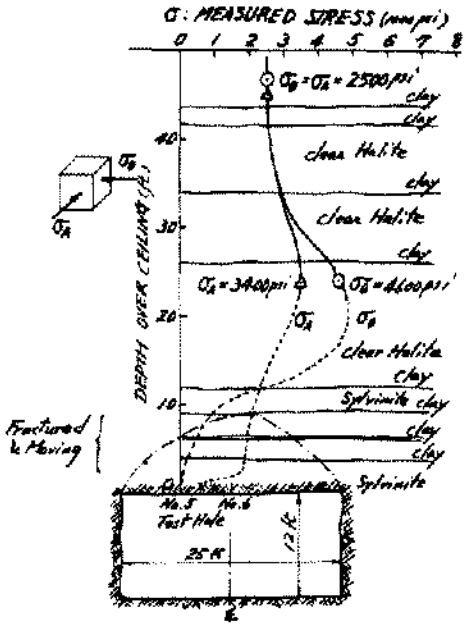

Figure 40. Stress distribution in test hole no. 5 over failed roof in potash mine opening at depth of 3,400 ft.

The sliding eventually closed the test hole while the Creepmeter was still in place, almost trapping it. The distribution of the lateral stress determined in Test Hole 5 is summarized in Figure 40.

The lateral stress at the depth of 47 feet was computed to be 2,580 psi on the average which gives the P_L/P_o ratio of 76.0%. This value comes very close to the two other values obtained in Test Hole No. 1. The minimum limit of the lateral stress for the ultimate stable state was given as,

$$\sigma_L = \sigma_z \cdot \frac{3\,G_2\,K_0}{\sqrt{2}\,(G_1 + G_3)}$$

The value was computed to be 2,700 psi, which gives the P_L/P_o ratio of 79.4%.

At the depth of 24 feet, the tangential stress response was greater than the axial stress response shown in Figure 40. By assuming the top of the stress arch over the opening to be at the depth of 24 feet, the stress distribution curve of Figure 40 was constructed. A number of measurements were made in the region between 6 and 11 feet, in order to locate the lower edge of the stress arch in this depth range. Altogether 10 observations were made in this range, but they failed to produce any meaningful result because of the continuous movement of the fractured roof and separations of layers.

Two stable measurements were made very close to the ceiling at the depth of 9 inches and 3.8 feet. At these two depths, the stress response was taken in the middle of separated slabs. Their response curves are characterized by a large positive response in the tangential direction, and an even larger negative response in the axial direction. The characteristics of the response indicate uniaxial stress acting in the tangential direction of the slabs.

The stress field in the halite and sylvinite formations of the mine was estimated from the overall evaluation of the above analyses as follows:

Overburden pressure: $P_o = 3400$ psi ± 100 psi

Uniform lateral stress: $P_L = 2600$ psi ± 100 psi

The ratio of P_L to P_o: $P_L/P_o = 76.5 \pm 7\%$

The stress field determined by the viscoelastic method in the halite and sylvinite formations at the depth of 3,400 feet in the Saskatchewan Prairie was found to be in agreement with the theory of underground stress field. The theory predicted the

lateral stress at the test site to be in the range from 1,300 psi to 5,500 psi regardless of the direction and magnitude of the existing tectonic stress. The existing earth lateral stress was found to be at the lower limit of the ultimate stable state, i.e., 2,700 psi. This indicates that there is no compressive tectonic force acting in the formation. These findings are in excellent agreement with the results of another underground investigation previously conducted in a neighboring potash mine operating in the same ore formation. The previous study was made by lone-term observation of the viscoelastic deformation around a 21 foot diameter mine shaft. The deformation was analyzed for both the diameter change and internal strain distribution in the rock medium surrounding the shaft.

The stress distribution determined over the mine opening illustrates how the opening establishes a stable equilibrium condition after having suffered extensive failure of the immediate roof. The nature of the stress distribution indicates that a stress arch is formed over the fractured roof at the depth of at least 24 feet above the original ceiling level. This is considerably deeper than those of stress arches commonly formed over competent roofs in the mine. Thus, the depth of the stress arch seems to have increased following the failure of the immediate roof.

No effect of the roof failure was found at the depth of 47 feet. The stress distribution at this depth was the same as the natural stress field of the formation prior to the mining. This stress distribution may be regarded as positive evidence of the mine's safety against potential flooding from the waterbearing formation which lies within 50 feet from the ceiling. The viscoelastic method of determining stress field by using the Borehole Creepmeter has many advantages over other conventional methods of in-situ stress determination. It is more reliable in rocks which do not conform to ideal elasticity. The method is practical in underground mines because of its speed, and simplicity in operation as it does not require overcoring. The method is particularly suitable for stress determination of deep underground formations by using test wells. Such field investigations have been carried out in depths up to 10,300 feet. The viscoelastic method would be applicable even at a shallow depth if the K_o-value of the formation is sufficiently small for viscoelastic deformation of the borehole.

CONCLUSIONS

1. The successful development of a finite element program which is useful for analysis of solution cavities and conventional salt mines is solely dependent upon the constitutive equations of rock salt based on the tensor analysis of the material in the laboratory.

2. There is a significant difference in the behaviors between solution cavities and conventional salt mines which is attributed to the effects of temperature and geometry difference.

3. A finite element program developed for solution cavities should be examined and calibrated by using a model cavity of a thick-walled cylinder.

4. A finite element program developed for conventional mines should be examined and calibrated by using a three-dimensional laboratory model which provides observation of various model structures under strict three-dimensional control.

5. A borehole drilled through the salt formation in which solution cavities are to be created should be used for in situ determination of the underground stress field to which the finite element program should be calibrated.

6. Time-dependent behaviors of relatively simple mine structures should be observed in order to calibrate the finite element program of the mines.

7. A Borehole Creepmeter was developed for insitu determination of the stress field to be used for stress distribution analysis of conventional salt mine structures.

8. A finite element program which is examined and modified through laboratory and field calibration can be used for "computer experimentation" of solution cavities and conventional mine structures.

ACKNOWLEDGMENT

The author acknowledges the able assistance of the staff engineers of Serata Geomechanics, specifically, Toshihisa Adachi in the theoretical analysis, Yuzo Ohnish in the computer analysis and Yoshi Tomozawa in laboratory testing. The author expresses his deep gratitude to the following companies who supported various phases of this work. International Salt Co., Wyandotte Chemical Corp., Texas Gulf Sulphur Co., and U.S. Borax Co.

REFERENCES

Adachi, T., Serata, S., and Sakurai, S., 1969. Determination of Underground Stress Field Based on Inelastic Properties of Rocks, 11th Symposium on Rock Mechanics, Berkeley, Calif., University of Calif.

Bieniawski, Z.T., 1967, Mechanism of Brittle Fracture of Rock, International Journal of Rock Mechanics and Mining Sciences, v. 6, no. 2, p. 395-406.

Drueker, D.C., 1959, A Definition of Stable Inelastic Material, Jour. of Applied Mechanics, Trans. ASME, v. 81, Series E, p. 101-106.

Reiner, R.F., 1960, Plastic Yielding in Anelasticity Journal of Mechanics and Physics of Solids, v. 8, p. 255-261.

Serata, S., 1964, Theory and Model of Underground Openings and Support System, Proceeding of the 6th Symposium on Rock Mechanics, University of Missouri at Rolla.

——, 1968, Application of Continuum Mechanics to Design of Deep Potash Mines in Canada. Int. Jour. of Rock Mech. and Mining Sci., v. 5, p. 293-314.

Serata, et. al., 1962-1966, Principles of Stress Fields in Underground Formations, NSF Project G-19791 & GP-2646, Progress Report Nos. 2, 4, 5, 6, 7 & 8., Div. of Eng'g. Research, Michigan State University, East Lansing, Michigan.

Serata, S., Sakurai, S., and Adachi, T., 1968, Theory of Aggregate Rock Behavior Based on Absolute Three-Dimensional Testing of Rock Salt. Tenth Symposium on Rock Mechanics, Univ. of Texas, Austin, Texas.